LA-UR-14-27904 (Accepted Manuscript)

Numerical modeling of injection, stress and permeability enhancement during shear stimulation at the Desert Peak Enhanced Geothermal System

Dempsey, David Edwin
Kelkar, Sharad M.
Davatzes, Nick
Hickman, Steve
Moos, Dan

To be published in: International Journal of Rock Mechanics and Mining Sciences

DOI to publisher's version: 10.1016/j.ijrmms.2015.06.003

Permalink to record: http://permalink.lanl.gov/object/view?what=info:lanl-repo/lareport/LA-UR-14-27904

IJRMMS-D-14-00457 – edited and approved by editor

Numerical modeling of injection, stress and permeability enhancement during shear stimulation at the Desert Peak Enhanced Geothermal System

David Dempsey[a*], Sharad Kelkar[a], Nicholas Davatzes[b], Stephen Hickman[c], Daniel Moos[d]

[a]Los Alamos National Laboratory, Los Alamos, NM, USA
[b]Temple University, Philadelphia, PA, USA
[c]USGS, Menlo Park, CA, USA
[d]Baker Hughes Inc., Palo Alto, CA, USA

[*]Corresponding author
Department of Geophysics, Stanford University, Stanford, CA 94305-2215
Tel: 001 505 310 1299
e-mail: dempsey7@stanford.edu

Abstract

Creation of an Enhanced Geothermal System relies on stimulation of fracture permeability through self-propping shear failure that creates a complex fracture network with high surface area for efficient heat transfer. In 2010, shear stimulation was carried out in well 27-15 at Desert Peak geothermal field, Nevada, by injecting cold water at pressure less than the minimum principal stress. An order-of-magnitude improvement in well injectivity was recorded. Here, we describe a numerical model that accounts for injection-induced stress changes and permeability enhancement during this stimulation. We use the coupled thermo-hydrological-mechanical simulator FEHM to: (i) construct a wellbore model for non-steady bottom-hole temperature and pressure conditions during the injection, and (ii) apply these pressures and temperatures as a source term in a numerical model of the stimulation. A Mohr-Coulomb failure criterion and empirical fracture permeability is developed to describe permeability evolution of the fractured rock. The numerical model is calibrated using laboratory measurements of material properties on representative core samples and wellhead records of injection pressure and mass flow during the shear stimulation. The model captures both the absence of stimulation at low wellhead pressure (WHP $\leq$1.7 and $\leq$2.4 MPa) as well as the timing and magnitude of injectivity rise at medium WHP (3.1 MPa). Results indicate that thermoelastic effects and the non-local stresses arising from these combine to propagate a failure front away from the injection well. Elevated WHP promotes failure, increases the injection rate, and cools the wellbore; however, as the overpressure drops off with distance, thermal and non-local stresses play an ongoing role in promoting shear failure at increasing distance from the well.

Keywords
Desert Peak; shear stimulation; permeability enhancement; thermal stress; modeling

1 Introduction

Shear stimulation is one method for improving the permeability of naturally fractured rock to create an Enhanced Geothermal System (EGS). The approach is an evolution of the idea that, over geological time, shear slip is necessary to create and maintain the conductivity of naturally-occurring fractures and faults [1 2]. EGS stimulations are designed to accelerate this process – inducing shear failure on existing fractures – through injection of cold water, thereby elevating fluid pressure inside the fractures and promoting cooling and thermal contraction of the fracture walls. Frictional failure induced by these fluid pressure and stress changes combined with mismatch of asperities during shearing results in self-propped, dilatant fractures that are better able to conduct fluids. Additionally, creation of new flow paths grows the fracture network, increasing the volume of rock amenable to heat extraction.

The success of this approach relies on the existence of hot rocks containing fractures oriented for shear failure, ambient differential stress large enough that the fractures are already near frictional failure, and material and mechanical properties conducive to shear-enhanced dilation [3]. Such conditions are frequently found in or adjacent to natural hydrothermal systems [4 5], which are often associated with regions of tectonic extension (leading to critically stressed fractures under low confining stress) and lithospheric thinning (for high crustal temperatures at drillable depths). In addition, fluid-rock interactions in natural hydrothermal systems can either promote shear-enhanced dilation through rock silicification and embrittlement [6], or inhibit dilation through clay alteration within fractures, favoring ductile deformation [5 7]. For these reasons, the margins of natural hydrothermal systems are convenient test beds for EGS shear stimulation operations, such as at Desert Peak, Nevada [8], Geysers, California [9], and Ngatamariki, New Zealand [10].

Shear stimulation is also utilized in conventional hydrothermal settings, for example, New Zealand [10] and the Philippines [11]. It has been noted that the injectivity of wells used for reinjection of produced fluids generally increases with continued use. As the reinjected brine is often cooler than the formation into which it is being injected, improvements to injectivity are in some cases attributed to thermoelastic contraction of rock mass around the well, leading to an increase in fracture apertures under decreasing normal stress. This elastic mechanism is in marked contrast to the shearing-induced changes in permeability discussed above, and is consistent with reports of injectivity decline when reinjection is halted or a well is subsequently produced [10].

Numerical simulators that account for the coupled thermal-hydrological-mechanical (THM) processes involved in an EGS shear stimulation are becoming increasingly widespread, and include FEHM [12], TOUGH2-FLAC3D [13], OpenGeoSys [14 15] and FALCON [16]. In addition to accounting for two-phase fluid flow and heat transfer, these codes solve force balance equations for stress and deformation on a continuum representation of the matrix-fracture domain. It is particularly important to capture thermoelastic and poroelastic stress changes induced in the rock matrix when cold water is injected at elevated pressure into a hot reservoir; these induced stresses can lead to permeability enhancement by promoting frictional failure or elastic fracture dilatation, compounding the direct effects of changes in effective normal stress on fracture permeability.

To model properly injectivity enhancement during stimulation requires relationships for the change in permeability in response to the perturbed stress state, including both elastic and inelastic effects. These relationships include elastic opening of fracture apertures through reduction of effective normal stress by fluid pressurization [17] or changes in thermoelastic stress due to cooling [10]; in both cases, injectivity gains can be lost when the reservoir reverts to its original state. Alternatively, plastic deformation upon mechanical failure can lead to permanent permeability gains. Several conceptual models and mathematical formulations have been proposed for stress-dependent fracture permeability during fluid pressurization. These models include thermo-poroelastic deformation of a regular array of fractures [18], aperture enhancement through fracture-propagation and shear-dilation of a statistically representative fracture population [19], a crack-tensor approach that yields upscaled permeability and elastic properties based on Mohr-Coulomb failure and dilation of sub-grid-scale fractures [20], and permeability as a function of the normal-stress dependent fracture aperture [21].

In this paper, we present a THM numerical modeling study of the shear stimulation of well 27-15 in the Desert Peak geothermal field, Nevada. Similar to the crack-tensor approach of Rutqvist et al. [20], we use sub-grid-scale fracture populations that are assessed for Mohr-Coulomb failure, with permeability enhanced according to an empirical relationship based on laboratory shearing experiments. In Section 2, we discuss the tectonic and structural setting at Desert Peak, and summarize the comprehensive site characterization studies that reveal the distribution of pre-existing fractures, the orientations and magnitudes of ambient stresses, and the lithological and mechanical properties of the stimulated formations. We also summarize key aspects of the multi-staged shear stimulation [3, 8] carried out at this site. In Section 3, we describe the construction of a numerical wellbore model used to determine non-steady bottom-hole temperature and pressure conditions during this shear stimulation. In Section 4, we describe construction of the shear stimulation model including the relationship for

stress-dependent permeability and a time-varying injection source term informed by the wellbore model. In Section 5, we present the calibrated stimulation model for Desert Peak EGS well 27-15 and discuss spatial and temporal evolution of the stimulated region along with model sensitivities. The coupled THM modeling study presented here builds on earlier work by Kelkar et al. [22] and Dempsey et al. [23 24].

2 The Desert Peak EGS demonstration project

2.1 Site characterization

Natural hydrothermal systems in the Great Basin of the western United States generally are found within several northeast trending belts that are aligned orthogonal to the direction of extension [25]. These regions localize extensional deformation and crustal thinning, which opens pathways for deep fluid circulation and advective heat transfer to shallower depths. The Hot Spring Mountains are located in one of these belts - the Humboldt Structural Zone - and host three major geothermal fields: Desert Peak, Brady's and Desert Queen. Desert Peak is a high-enthalpy, blind geothermal system with no active hot springs or fumaroles. The field is associated with a left step in the NNE-trending, WNW-dipping Rhyolite Ridge normal fault zone [25]. The orientation and mode of faulting are consistent with regional NW-directed extension [26].

Geothermal power is generated from fluids produced in the southwest region of the Desert Peak field, with additional pressure support for the reservoir supplied by reinjection into several wells northeast of the main production area (Figure 1). When drilled, well DP 27-15 exhibited poor injectivity and was selected for EGS stimulation over three potential depth intervals [27]. The uppermost of these zones was selected for an initial (shallow) stimulation, extending from the casing shoe at 915 m to the top of a temporary cement plug at 1065 m. This cement plug was later drilled out and in order to allow the entire open-hole interval of 27-15 stimulated in the final phase of the Desert Peak EGS project. This latter phase of the project will not be discussed further in this paper. The shallow stimulation consisted of three phases [8]: (i) shear stimulation by injection of cold-water at pressure less than the minimum horizontal principal stress, σ_h; (ii) chemical stimulation by injection of acid; and (iii) a controlled hydraulic fracturing phase. Only the shear stimulation phase is modeled here; a discussion of the other shallow stimulation phases is presented in Chabora et al. [8]. Prior to this stimulation, comprehensive borehole geophysics, tracer studies, laboratory testing and seismological studies were undertaken to create a geomechanical and hydrologic model of the site [3 7 27-29].

Shear stimulation relies on the triggering of self-propping shear failure on pre-existing fractures. In designing and modeling the effects of a shear stimulation, it is necessary to know the pre-existing fracture distribution, including orientations, density and frictional properties, and the magnitude and orientation of the in-situ principal stress fields acting on those fractures. Davatzes and Hickman [27] undertook a fracture characterization study in well 27-15 using borehole image logs collected to depths of almost 1700 m. They recorded extensive drilling-induced tensile failure that indicated an orientation for σ_h of 114$\pm$17°, consistent with the NNE trend of surface normal faulting [30]. Temperature gradient anomalies from precision temperature logs were also used to identify zones of fluid flow, interpreted to correspond to intervals of slightly elevated fracture permeability.

In an extensional tectonic setting, the maximum principal stress, σ_v, is typically assumed to be vertical and equal in magnitude to the overburden. For well 27-15, σ_v was calculated from a lithological profile determined by cuttings analysis, in concert with density testing of core taken from the nearby well 35-13 The magnitude of σ_h at the top of the stimulation interval was determined from the stable instantaneous shut-in pressure obtained from a small-volume, low-flow-rate hydraulic fracturing test, corroborated by a step-rate injection test [3]. The magnitude of σ_h at the mid-point of the mini-hydrofrac interval (930$\pm$12.5 m) was 13.8$\pm$0.4 MPa. At this same depth, σ_v was calculated to be 22.6 MPa, yielding a ratio of σ_h/σ_v of 0.61$\pm$0.02 [3]. Ambient formation pressure was estimated from a static temperature/pressure/spinner (TPS) log and found to be 7.5 MPa at 930 m, corresponding to a water table 116 m below the ground surface. Hickman and Davatzes [3] constrain the magnitude of the intermediate principal stress, σ_H, using two possible stress models: normal faulting and transitional normal to strike-slip faulting. These yield an upper bound of $\sigma_H = \sigma_v$ and a lower bound of $\sigma_H = (\sigma_v + \sigma_h)/2$.

Mechanical testing on core samples from well 35-13 was performed to determine mechanical properties such as Young's modulus, Poisson's ratio, permeability and intact and fracture frictional properties of the relevant rock types [7]. Three rhyolite tuffs and two metamorphic basement units with varying degrees of hydrothermal alteration and clay content are identified in the stimulation interval. The dominant argyllic and siliceous rhyolites and illitic metamudstone units have measured porosities of ~10% and matrix permeabilities from 0.02 to 40 milliDarcy (2×10^{-17} to 4×10^{-14} m^2). The coefficient of friction measured during quasi-static sliding of fractured rock samples ranges from 0.65 for the argyllic rhyolite to 0.96 for the siliceous rhyolite and illitic metamudstone; this range of friction values was used by Hickman and Davatzes [3] to constrain their geomechanical model of the Desert Peak field. In the shear stimulation model presented in Section 4, we use a friction coefficient of 0.75.

In a normal faulting stress environment, optimally-oriented, cohesionless fractures will fail when the magnitudes of σ_h, σ_v and formation fluid pressure, P satisfy the Mohr-Coulomb failure criterion for an appropriate value of the coefficient of friction, μ, [31]

$$\sigma_h = (\sigma_v - P)/\left((\mu^2 + 1)^{\frac{1}{2}} + \mu\right)^2 + P. \quad (1)$$

During the Desert Peak shear stimulation, WHP was increased in steps with the goal of increasing P in the formation until Eq. (1) above was satisfied. Decomposing the formation pressure into ambient and overpressure components, i.e., $P = P_0 + \Delta P$, and substituting into (1) above, we can calculate a range of WHPs within which the onset of shear stimulation should be observed. Taking σ_v=22.6 MPa, σ_h=13.8$\pm$0.4 MPa, P_0=7.5 MPa, and μ=0.65 to 0.96, we obtain the critical overpressure range above which stimulation should be expected to occur, ΔP_{crit}=2.1 to 4.8 MPa. Hickman and Davatzes [3] calculated that failure should be induced on pre-existing fractures for excess formation pressures greater than 2.5 MPa. It is important to note that ΔP experienced by the formation is not only the applied WHP, but also includes a 1.1 MPa contribution due to the weight of fluid required to fill the borehole, i.e., offset a water table at a depth of 116 m, and an additional component that increases as the borehole water cools with time due to the accompanying density increase. While these effects are neglected in the analysis presented above, they are accounted for in the models described in Sections 3 and 4.

On the basis of the in situ stress and fracture failure analyses of [3], it was determined that stimulation of DP 27-15 by cold-water injection should proceed with WHP being stepped in increments of 100 psi (~0.7 MPa) while staying below σ_h to avoid hydraulic fracturing – this imposes an upper limit on the WHP of 5.2 MPa [8]. Shear stimulation was undertaken at four pressure steps; WHP $\leq$1.7, $\leq$2.4, $\leq$3.1 and $\leq$3.7 MPa. Allowing for an additional 1.1 MPa due to filling of the borehole, overpressure in the formation, ΔP, will exceed the lower threshold for frictional failure, ΔP_{crit}, at all pressure steps.

2.2 Shear stimulation phase

The efficacy of EGS stimulations is generally quantified in terms of an increase in the injectivity of the well through which cold water is being pumped into the formation. In [8] and as summarized below, injectivity during the Desert Peak EGS stimulation is defined as the injection rate divided by the wellhead pressure (WHP). Alternative definitions may divide injection rate by the downhole overpressure (i.e., pressure in excess of undisturbed formation pressure) or take into account the

geometry of the stimulated volume as well as fluid viscosity changes; however, as these in-situ properties can be difficult to determine, the WHP definition is preferred. For a given WHP, an increases in formation permeability will result in a larger injection rate and, thus, a larger injectivity.

Injection rate and injectivity during the shear stimulation are summarized in Figure 2. Injection of ~30°C fresh water commenced at WHP $\leq$1.7 MPa resulting in injection rates of 0.2 to 0.3 kg s^{-1} and a calculated injectivity (based on WHP) of ~0.1 to 0.15 kg s^{-1} MPa^{-1}. During the second step, injection at a WHP $\leq$2.4 MPa resulted in injection rates of 0.25 to 0.4 kg s^{-1}, again corresponding to an injectivity of ~0.1-0.15 kg s^{-1} MPa^{-1}. During both pressure steps injectivity was stable for the 8 to 9 day injection period. While failing to achieve the goals of the stimulation, reproduction of this null result was nevertheless an important step both in demonstrating the existence of a critical pressure threshold for EGS shear stimulation and in calibrating the numerical model presented in this paper.

On September 13, 2010, injection recommenced at an increased WHP of 3.1 MPa. The initial injection rate was stable and averaged 0.4 kg s^{-1} for the first 4 to 5 days. The stable injectivity during this time, 0.13 kg s^{-1} MPa^{-1}, is consistent with that calculated for the previous pressure steps. Continued injection at nearly constant WHP was accompanied an initial rapid increase in injection rate which slowed with time. A rate of 4.4 kg s^{-1} was reached at the end of this stimulation step. Injectivity increased by a factor of 10 to 15 during this period, reaching a maximum of ~1.5 kg s^{-1} MPa^{-1} before injection was terminated after 38 days.

Following a 17-day shut-in, injection recommenced at the same WHP of 3.1 MPa for an additional 15 days. It was noted that, during the interim shut-in, injectivity had decreased by approximately a factor of 2 to a value of about 0.7 kg s^{-1} MPa^{-1}; however, by the end of this additional 3.1 MPa stimulation, injectivity had once more increased to 1.3 to 1.4 kg s^{-1} MPa^{-1}. Another 22-day shut-in was followed by injection at the final WHP of 3.7 MPa for 9 days. Once again, injectivity had decreased during shut-in to an initial value of 0.7 kg s^{-1} MPa^{-1}, but returned to a value of 1.4 kg s^{-1} MPa^{-1} by the end of the 9-day stimulation.

During the shear stimulation phase, only one microearthquake was detected [8]. However, as the detection threshold of the monitoring network during this phase was M_w ~0.5, the occurrence of lower-magnitude events cannot be ruled out.

2.3 Injectivity loss

The Desert Peak stimulation plan called for a phase of chemical stimulation by acid injection to follow the shear stimulation phase. The chemical stimulation showed no net improvement to injectivity

and is not part of the modeling study presented here. However, prior to beginning chemical stimulation, an injection test was performed on well 27-15, which had been shut in for approximately 45 days since the conclusion of the shear stimulation phase. This test indicated that injectivity had dropped to ~0.35 kg s^{-1} MPa^{-1}, a reduction of about a factor of four since the well had been shut-in. This result, in addition to similar declines in injectivity when the well was shut in between the shear stimulation steps (discussed above), indicates that a significant part of the stimulated injectivity in well 27-15 was not permanent. This experience is consistent with other reports of operation and stimulation of geothermal injection wells. For example, Grant et al. [10] have compiled productivity and injectivity measurements for 35 dual-use wells in New Zealand geothermal fields and calculated the ratio of injectivity to productivity for each. For 30 of these wells, the ratio of injectivity is greater than one (range: 1.2 to 21) for the same wells under conditions of injection compared to production. This behavior is attributed to an increase in fracture apertures either by thermal contraction when the surrounding rock mass is cooled by injected cold water or in response to injection-elevated fluid pressures within those fractures [17 32]. In either of these scenarios, the mechanism for injectivity gain is reversible.

In the case of shear stimulation in hard rocks, however, where self-propping shear failure is responsible for permeability enhancement, inelastic processes may contribute to permeability loss with time. For example, creep fracture closure through crystal plastic deformation or intergranular pressure solution along loaded asperities [13 33], or chemical precipitation in newly-sheared fractures [34 35], could result in a loss of fracture permeability. Such mechanisms are not included in the model described here. In numerical simulations, Taron and Ellsworth [13] reported aperture reduction of 40% over a one-year period by pressure solution alone. Martin and Lowell [34], modeling precipitation of silica in open fractures (applied to seafloor hydrothermal systems – black smokers), found that permeability reduction by this mechanism occurs over decade-long timescales. The relative importance and timescales over which these mechanisms operate is likely to vary from site to site due to differences in temperature (ambient and during injection), mineral assemblage, water-rock interaction, in-situ stress state, and initial permeability. At Desert Peak, it is possible that both elastic and inelastic processes contribute to the loss in permeability between stimulation phases; however, none have been explicitly considered in our modeling study.

3 Numerical simulation of wellbore cooling

This modeling study comprises two parts: (i) a wellbore model that predicts temperature and pressure conditions at the stimulation depth based on surface temperature of the injected fluid plus

borehole injection rate and heat transfer between the well and surrounding rock; and (ii) a reservoir stimulation model for temperature, pressure, stress and permeability at points of fluid egress from the well. Both models are constructed using the coupled thermal-hydrological-mechanical (THM) code Finite Element Heat and Mass transfer (FEHM) [36 37], although model domain and functionality are tailored to the specific problem. In this study, we do not account for injectivity loss during shut-in; as such, the model is only applied to the first three WHP steps corresponding to the first 67 days of the stimulation.

FEHM solves for Darcy heat and mass fluxes, and mechanical stresses and displacements in a deformable porous medium. The governing equations for mass, energy and stress balance are [12]

$$\begin{gathered}
\frac{\partial}{\partial t}(\rho\theta\phi) + \nabla \cdot q = Q_m, \\
q = -\frac{k k_r(\theta)\phi}{\mu}\nabla(P - \rho g z), \\
\frac{\partial}{\partial t}(\rho U\phi + (1-\phi)\rho_r C_r T) + \nabla \cdot (q\rho H) \qquad (2) \\
-\nabla \cdot (\Lambda \nabla T) = Q_e, \\
\nabla\sigma + \rho_r b = 0, \\
\sigma = \lambda tr(\epsilon)I + 2\mu\epsilon + (\beta\Delta P + \alpha E\Delta T)I \\
\epsilon = \frac{1}{2}[\nabla u + (\nabla u)^T]
\end{gathered}$$

where ρ, μ, U, and H are the density, viscosity, internal energy and enthalpy of the fluid, ϕ, ρ_r, C_r, Λ, and k are the porosity, density, specific heat, thermal conductivity and permeability of the rock, Q_m and Q_e are mass and energy source terms, θ and $k_r(\theta)$ are the saturation and saturation-dependent relative permeability, σ and b are the stress tensor and body force vector (typically $(0,0,g)$ for geological applications), ϵ and u are the strain tensor and displacement vector, λ, μ, E, α and β are Lame's parameters, Young's modulus, the coefficient of the thermal expansion and the Biot coefficient, g is gravity, and P and T are pressure and temperature. In the stimulation model, permeability is calculated as a function of σ (Section 4.1), which is then updated at the end of each time step.

The purpose of the wellbore model is to establish time-varying temperature and pressure for fluid injected into the formation. Injection temperatures at the wellhead were relatively stable at 20-30°C during the stimulation periods, although the injection rate varied from 0.1 kg s^{-1} at early times to 3-5 kg s^{-1} as the stimulation proceeded. Down-hole fluid temperature may be in equilibrium with the initial formation temperature at early times; however, as the near wellbore region cooled, and as injection rate into the well increased, the down-hole temperature declined relative to the far field surrounding formations.

One consequence of a cooling column of water inside the wellbore is that fluid density, and thus down-hole pressure, increases. For example, 190°C formation fluid at a pressure of 7.5 MPa has a density of 880 kg m^{-3}, approximately 12% less than cold surface water. In contrast, the density of cold-water inside the well will be higher, and the weight of the hydrostatic column proportionally greater. Thus, fluid pressure at the base of the well, once cooled, will exceed that in the formation even in the absence of an applied WHP. To complicate matters, this additional overpressure is not constant, but rather varies according to the temperature profile inside the well, which changes with time due to wellbore cooling and in response to increasing injection rates. Due to the complex nature of these feedbacks, a numerical model is required to estimate non-steady down-hole temperatures (DHT) and pressures (DHP).

3.1 Model construction

The wellbore model is summarized schematically in Figure 3A. Fluid entry into the wellbore occurs at the top of the model and fluid exit is assumed to occur at a single point of egress at a depth of 1030 m; this is near to the center of the fluid loss interval observed following the shear stimulation [8]. The full length of the injection well, from the surface to the point of fluid egress, is considered embedded in and in contact with high-temperature rock, the distribution of which is determined by a static temperature profile measured in the well (Fig. 3B; [29]). Heat transfer from the rock to the fluid occurs via conduction through the cement and casing. Cooling of the rock due to advection of cold fluid into the formation between the bottom of casing and the fluid egress point is not considered. The fluid flow in the wellbore is taken to be laminar.

The two-dimensional computational domain is meshed using a radial grid extending 1 km away from the borehole and to the injection depth of 1030 m. A variable mass flow water source is applied at the top of the wellbore with temperature and flow rate of the injected fluid (Fig. 3C-D) given by field data from the first three pressure stimulations (WHP $\leq$1.7, 2.4 and 3.1 MPa). This includes periods in which the well was shut in and no injection occurred. The injected water travels down the well, in thermal contact with the borehole wall, and is removed at the base of the well at the same rate it is injected at the top.

Representative thermal properties for the steel, cement and reservoir rock are given in Table 1. The wellbore model is calibrated against two temperature profiles taken during the stimulation. The first (Fig. 4B, red curves) was a static temperature profile obtained after a 12-day shut-in following the second 3.1 MPa stimulation; for this profile, the model successfully captures the degree of reheating

within the wellbore. The second profile (blue curve) was measured after a short period of injection following the 12-day shut-in; here, the model captures the magnitude of cooling in the wellbore.

3.2 Model results

For the two lower pressure stimulations (≤1.7 and ≤2.4 MPa), and at the beginning of the medium pressure stimulation (3.1 MPa), the injection rate is relatively low; consequently, the down-hole temperature remains high, between 150 and 190°C. Injection temperature drops rapidly between 30 and 40 days as the stimulation proceeds and injection rates increase. It stabilizes between 40 and 60°C for the remainder of the stimulation.

Several sharp rises are predicted in bottom-hole temperature (Figure 4A); these occur during pumping gaps in the 3.1 MPa stimulation. This is due to a rapid reheating at the base of the modeled wellbore because the reservoir temperature at this depth is still quite high. In practice, the injected fluid exits the wellbore into the formation and should lead to a much greater convective cooling of the surrounding rock than is captured by the wellbore model. Hence, the degree of reheating exhibited at the base of the wellbore is probably excessive. However, this argument does not apply to the rest of the wellbore; here, modeled reheating is reasonably accurate, as indicated by the close match between the modeled wellbore temperature and the static temperature profile in Figure 4A. The rapid temperature increases during modeled shut-in phases are not applied to the reservoir model.

The additional overpressure attributed to a cold versus hot hydrostatic fluid column is calculated by integrating the temperature dependent fluid density, ρ, from the surface to the injection depth, z_{inj}, and subtracting the down-hole pressure at ambient temperature conditions, P_0, obtained from equilibrated pressure logs, i.e.,

$$\Delta P = \int_{z_{inj}}^{0} \rho(T(z))\, g\, dz - P_0, \tag{3}$$

where g is the acceleration of gravity and the pressure dependence of ρ is neglected. The temperature dependence of water density is implemented in FEHM through a rational polynomial fit [36] to data from the NBS/NRC Steam Tables [38]. This additional overpressure is plotted in Figure 4C.

For the low pressure stimulations (≤1.7 and ≤2.4 MPa), where the injection rate is low and temperature in the wellbore is near the far-field value, the additional density correction is relatively small - ~10% of the applied WHP. However, this term increases rapidly between 30 and 40 days in concert with the drop in bottom-hole temperature. For the medium pressure stimulation, it retains a relatively high value of 0.5-0.6 MPa; this is approximately 20% of the applied WHP. This correction is

significant, particularly as WHP must be carefully managed within a narrow range so as to exceed the threshold for shear failure (2.1 to 4.8 MPa; Section 2.1) but not so much as to also exceed the threshold for hydraulic fracturing (5.2 MPa).

The modeled bottom-hole temperature and pressure sequences will be used in the next section as a forcing term for the stimulation model.

4 Reservoir model

In these simulations, shear stimulation of reservoir rock is captured by a stress-dependent elastic/frictional permeability model. In short, injection of medium-pressure, cold water changes in situ effective stresses, thereby increasing permeability through brittle (frictional) failure. The increase in permeability leads to a corresponding increase in injection rate under constant WHP conditions; this results in a positive feedback, whereby increased injection rates deliver more, colder water, resulting in further increase in permeability and an expanding region influenced by hydraulic stimulation.

We assume an extensional stress regime, with the principal stresses oriented parallel to a Cartesian axis, i.e., $\sigma_1 = \sigma_v = \sigma_Z$, $\sigma_2 = \sigma_H = \sigma_Y$, and $\sigma_3 = \sigma_h = \sigma_X$. This stress state is consistent with the tectonic setting and abundant normal faulting in the Desert Peak region [26 30]. The following sign and symbol conventions are used: (a) Stresses are positive in compression. (b) The global model and local fracture coordinate systems are denoted by upper (X, Y, Z) and lower case type (x, y, z), respectively. (c) Many of the calculations in this work involve the logarithm (base 10) of permeability. We refer to transformed and untransformed quantities using k and κ, respectively, i.e., $k = \log_{10}(\kappa)$.

4.1 Stress-dependent permeability

Our model for stress-dependent permeability is based on the concept of a ubiquitously fractured medium. Each control volume in the model – the region of space uniquely associated with a computational node – is assumed to contain a number of through-going, non-intersecting, non-interacting fractures of varying orientation. Each of these fractures has some initial permeability that can change according to the local stresses and a shear-slip (Coulomb) failure criterion. Nodal permeability is calculated as the ensemble sum of all fracture permeabilities, some of which may be enhanced from their original values. Thus, the operation of the permeability model mimics our conceptual understanding of the shear stimulation; fractures are brought to shear failure by the application of low-temperature, overpressured fluid.

Our method allows arbitrary complexity in the specification of fracture orientations. The distribution can contain any user-specified anisotropy or can be informed by field fracture observations, e.g., outcrop studies or bore-hole image logging. To better understand the existing permeability and stress state in the target formations at Desert Peak, bore-hole image logging of fractures in well 27-15 was undertaken prior to the shear stimulation [27]. The analysis yielded 72 fracture orientations in the stimulation interval; the distribution (Figure 5A) exhibits a low-degree of anisotropy, with a slightly higher density of fractures well-oriented for reactivation in the prevailing stress field. This naturally occurring orientation bias is one source of permeability anisotropy in our model.

As fracture orientations vary within a population, so too do the resolved magnitudes of τ and σ_n on each fracture. The sub-set of fractures oriented such that stress conditions are closest to failure constitutes the optimally-oriented or stress-sensitive fractures [39]; these are generally the first to fail during stimulation. For an extensional stress regime and a friction coefficient of 0.6, the optimally-oriented fractures dip at 60° and strike parallel to the maximum horizontal principal stress, σ_H. Preferential reactivation of these fractures will result in a greater permeability enhancement parallel to σ_H; this is the second source of anisotropy in the model.

Knowledge of pre-existing fracture orientations is incorporated into the synthetic fracture populations that are generated by the model. The algorithm for constructing these populations is based on sampling a density map constructed from observations of fracture orientations and is outlined below. First, the hemisphere represented by the stereonet in Figure 5A is decomposed into M equal-area, evenly-distributed, overlapping spherical caps. Fracture orientation density, in a per-steradian sense, is calculated for each sub-region. For the Desert Peak data, a value of $M = 200$ provides a reasonable discretization. However, increased sub-division can improve resolution of the density map where there is sufficient data. Next, a total of N synthetic fractures orientations are distributed amongst the M hemisphere sub-regions in proportion with the compiled density map. Thus, sub-regions with more fracture observations are assigned a higher number of synthetic fractures. Within each sub-region, fracture orientations are randomly distributed.

At the beginning of each simulation, a different set of N fracture orientations is constructed and assigned to each computational node. Each fracture population is retained for the duration of the simulation; we do not consider the creation of new fractures or stress interactions between proximal fractures undergoing shear.

All fractures in the model experience and respond to both ambient and induced stresses. Failure of each fracture is assessed in terms of the Mohr-Coulomb criterion, which is here formulated in terms of the excess shear stress, τ_{ex}, which describes the proximity to failure,

$$\tau_{ex} = |\tau| - \mu_s(\sigma_n - P) - S_0, \quad (4)$$

where τ and σ_n are the shear and normal stress on the fracture, P is the fluid pressure in the fracture, and μ_s and S_0 are the static coefficient of friction and cohesion. Modifications to the stress field on a sub-grid scale due to fracture failure are not considered in this work.

Excess shear stress is generally less than zero for stable fractures, which indicates the current shear stress on the fracture is too small to overcome the combined stabilizing influence of static friction and cohesion. As τ_{ex} approaches zero, the fracture becomes critically stressed; when it reaches zero, the fracture fails. Eq. (4) encapsulates two of the mechanisms contributing to this failure in our model: (i) an increase in fluid pressure within the fracture; and (ii) a decrease in the normal stress due to cooling.

In practice, when a fracture fails in shear, the shear stress on the fracture drops, a shear displacement occurs, and τ_{ex} drops below zero again. Fracture cohesion may decrease or become zero at this time. However, this post-failure behavior is not fully represented in the model because fractures are not explicitly meshed. Instead, the stress drop and shear displacement are inferred from the continuum stress solution.

Stress drops are calculated using a static/dynamic friction model [40-42]. Upon failure, it is assumed that the fracture becomes cohesionless and that the friction coefficient drops to some lower dynamic value, μ_d. In practice, slip would accumulate until the balance of forces, still governed by the Mohr-Coulomb failure criterion (Eq. (4)) but now with different parameters, is restored. The modeled stress drop, $\Delta\tau$, is given by

$$\Delta\tau = |\tau| - \mu_d(\sigma_n - p_f). \quad (5)$$

Stress drop is calculated only as an intermediate step to obtain permeability enhancement; in this work, the modeled stress solution, i.e., τ and σ_n, is not modified in response to failure. Thus, ongoing cooling or fluid pressure increases permit $\Delta\tau$ to continue increasing. This increase is taken as a proxy for continued shear displacement of a fracture, which is calculated by multiplying the stress drop by a fracture stiffness parameter, K, similar to the models of Hossain et al. [19] and Rutqvist et al. [20]. In practice, continued fracture displacements would likely be stick-slip in nature, with multiple smaller stress drops.

Changes in fracture permeability are based on an empirical relationship between shear displacement and permeability enhancement motivated by laboratory sliding experiments by Lee and Cho [43]. They made linear flow measurements on rough, artificial fractures, in granite and marble, for a variety of in situ stresses. As illustrated in Fig. 5B, increasing permeability enhancement with shear displacement was demonstrated for both rock types and was correlated with enlargement of the mechanical aperture by non-alignment of asperities. In these experiments, permeability approached a limiting value; this was attributed to asperity degradation or production of flow-inhibiting gouge. At high normal stress, the total permeability increase was less for marbles that for granites; this difference was attributed to the more extensive gouge production.

The poorly consolidated rhyolites that were the target of stimulation at Desert Peak differ from the granites and marbles tested by Lee and Cho [43]. Nevertheless, it is reasonable to suggest that the underlying physical processes leading to permeability enhancement in marble and granite, e.g., non-alignment of asperities, gouge production, also manifest in other lithotypes. While the relative importance of these processes may vary – for instance, brecciated rhyolites may produce rougher fracture walls – the general form of the relationship should be preserved. Thus, in this work, the Lee and Cho [43] model is used as a template relationship for shear displacement and permeability enhancement. A sigmoidal function is used to describe change in the logarithm of permeability, $\Delta \mathrm{k}$, as a function of shear displacement (Fig. 5C), u, i.e.

$$\Delta \mathrm{k} = \frac{\Delta \mathrm{k}_{\max}}{1+\exp\left(\ln(19).(1-2\frac{\mathrm{u}-\mathrm{u}_5}{\mathrm{u}_{95}-\mathrm{u}_5})\right)}, \quad (6)$$

where $\Delta \mathrm{k}_{\max}$ is the maximum change in permeability, and u_5 and u_{95} are the shear displacements at which $\Delta \mathrm{k}$ is 5 and 95% of the maximum. Because $\Delta \mathrm{k}$ is an absolute change in logarithmic-space, it corresponds to a multiplier of the untransformed permeability, i.e., $\kappa' = 10^{\Delta \mathrm{k}} \times \kappa$.

4.1.1 Ensemble averaging of fracture permeability

In applying the stress-permeability relationship, the model resolves stresses on each hypothetical fracture plane, evaluates the failure criterion, and infers a stress drop, shear displacement and associated change in fracture permeability. As a final step, we need to compute, for each node, a new permeability tensor in the global frame representing the effective permeability of all fractures associated with that node, stimulated or not.

In the local frame, the permeability tensor associated with the i^{th} fracture, $\mathrm{K}^{\mathrm{i}}_{\mathrm{frac}}$, is defined by two equal, in-plane components, κ_{i} – flow is assumed in the plane of the fracture only, thus, the out of plane

component is zero. When rotated to the global frame, K_{nd}^{i} has six resolved components. The transformation is given by

$$K_{nd}^{i} = \left(R^{i}\right)^{T} K_{frac}^{i} R^{i} = \left(R^{i}\right)^{T} \begin{bmatrix} \kappa^{i} & 0 & 0 \\ 0 & \kappa^{i} & 0 \\ 0 & 0 & 0 \end{bmatrix} R^{i}, \qquad R^{i} = \begin{bmatrix} l_x & m_x & n_x \\ l_y & m_y & n_y \\ l_z & m_z & n_z \end{bmatrix} \tag{7}$$

where the components of the rotation matrix R^{i} are the direction cosines of the local-frame basis vectors in the global frame. Fracture permeability is expressed in terms of an initial value, κ_0^{i}, and a multiplier, $c^{i}(\hat{n}) = 10^{\Delta k}$, where the multiplier is calculated based on fracture orientation (as defined by its normal, $\hat{n}$) as described in the previous section. Nodal permeability is obtained by averaging over the N fractures associated with the node, i.e.,

$$\kappa_{jj} = C_{jj}\, \kappa_{jj0} = \frac{1}{N} \sum_{i=1}^{N} r_{jj}^{i}(\hat{n}) c^{i}(\hat{n})\, \kappa_0^{i}, \tag{8}$$

where C_{jj} is a multiplier for overall nodal permeability in the j direction and $r_{jj}^{i}(\hat{n})$ is a term from the transformation between local and global frames, i.e., $r_{jj}^{i}(\hat{n}) = \left((R^{i})^{T} R^{i}\right)_{jj}$. Here, we assume initial fracture permeability is equal for all fractures, i.e., $\kappa_0^{i} = \kappa_0$,. This summation approach is similar to that implemented by Moos and Barton [39] in optimizing well productivity against orientation; however, here we omit Terzaghi's [44] geometric correction, used to account for the likelihood of intersection between a well and variously oriented fractures.

In this work, we include only the permeability components along the global axes, discarding the off-diagonal terms. This simplification is reasonable in situations where the eigenvectors of the permeability tensor are closely aligned with axes in the global coordinate system and where changes in permeability associated with stimulation do not generate large off-diagonal terms. In our case, due to a distribution of fractures that is only slightly anisotropic, and for which the fracture distribution leads to principal axes of the native permeability tensor that approximately align with the principal stress axes (Figure 5A) we can by aligning principal stresses parallel to the global coordinate axes ensure that off-diagonal components are small throughout the stimulation process.

For internal consistency with the ensemble averaging approach employed here, the initial nodal permeabilities must satisfy Eq. (8) with $c^{i}(\hat{n}) = 1$, i.e.,

$$\kappa_{jj0} = \frac{\kappa_0}{N} \sum_{i=1}^{N} r_{jj}^{i}(\hat{n}). \tag{9}$$

Thus, in our model, the initial permeability anisotropy is defined by the ensemble of fracture orientations, i.e.,

$$\kappa_{XX0} : \kappa_{YY0} : \kappa_{ZZ0} = \sum_{i=1}^{N} r_{XX}^{i} : \sum_{i=1}^{N} r_{YY}^{i} : \sum_{i=1}^{N} r_{ZZ}^{i} \tag{10}$$

For the set of fractures imaged at Desert Peak, the initial anisotropy calculated by (10) is 1 : 1.2 : 0.8, i.e., fractures are oriented such that there is a slight preference for flow parallel to the maximum horizontal principal stress. This finding is consistent with concepts of enhanced fluid flow on critically-stressed fracture meshes [45].

Finally, for the case that each fracture has the same initial permeability, assumed here, the nodal permeability multipliers are obtained by dividing Eq. (8) by Eq. (9)

$$C_{jj} = \sum_{i=1}^{N} r_{jj}^{i}(\hat{n}) c^{i}(\hat{n}) \Big/ \sum_{i=1}^{N} r_{jj}^{i}(\hat{n}) \ . \quad (11)$$

4.1.2 Demonstration of permeability enhancement

Before implementing this stress-permeability relationship in a model for the Desert Peak shear stimulation, it is useful to illustrate its behavior at the nodal level in response to stimulation conditions. We consider a target injection depth of 1000 m and in-situ stresses as determined in the Desert Peak EGS well 27-15, i.e., σ_v is lithostatic, $\sigma_h = 0.61\sigma_v$, and $\sigma_H = 0.5(\sigma_v + \sigma_h)$ [3]. For the material properties considered here, μ=0.6 and S_0=0, all fracture orientations are stable.

According to Eq. (4), failure can be caused by increasing fluid pressure within the fracture or decreasing normal stress through cooling. Functionally, the two are equivalent, so here we consider a steady ramping of the pressure to 15 MPa above its initial value. In practice, this would result in P exceeding σ_h resulting in hydraulic fracturing; however, for the purposes of demonstrating the permeability model this can be ignored. Increases in the three permeability multipliers over this range are plotted in Figure 5D. These curves reflect several features of the conceptual model, including:

1. Permeability enhancement is not immediate. Rather, some threshold forcing must be overcome before even the most stress-sensitive fractures are brought to failure.
2. Initial permeability enhancement is predominantly parallel to σ_H and σ_v. This is because the planes of stress-sensitive fractures – those first to fail – tend to contain σ_H and are steeply dipping.
3. In the hypothetical limit that pressure is sufficient to activate all fractures, all permeability multipliers converge. This does not suggest that permeability is now isotropic, only that there is no additional anisotropy supplied by the preferential activation of some fracture orientations and not others.

Stereonets plotted at three stages of pressurization in Figure 5D illustrate the concept of preferential activation of stress-sensitive fractures. At low pressure, only the fractures dipping at high

angles in the direction of σ_h are partially activated (the blue dots) while the others remain inactive (green). With increasing pressure, these orientations become fully activated (black dots), i.e., the limiting permeability is reached, while at the same time, less favorably-oriented fractures fail. Finally, at very high pressures, all fractures are activated.

It is worth noting that, permeability anisotropy related to the intrinsic distribution of fractures, i.e., $\kappa_{X0} > \kappa_{Z0}$ (Eq. (10)), does not coincide with the initial anisotropy in stimulated permeability, $\Delta k_Z > \Delta k_X$. The latter arises from preferential stimulation of stress-sensitive fracture orientations; thus, this distinction is illustrative of the complex relationships between ambient stress, intrinsic material properties and injection conditions created during shear stimulation. These considerations are important, for example, when selecting the optimum orientation of a deviated well, which will depend both on the available fracture orientations, as well as the subset that are critically stressed and thus likely to have high natural permeability [39].

The curves in Figure 5D represent anisotropic permeability enhancement for the Desert Peak fracture population. However, in our model, each node is associated with a unique fracture population that is informed by the Desert Peak population and is therefore associated with a unique set of permeability multiplier curves. Figure 5E illustrates 20 sets of such curves corresponding to 20 different synthetic fracture sets. These indicate that the features of the curves in Figure 5D are generally preserved, for example, greater immediate permeability gains in the σ_H and σ_v directions.

A similar approach was method for permeability enhancement was applied by Moos et al. [46] in modeling shear stimulation of a shale reservoir. However, in their model, permeability enhancement curves included a component of elastic dilation associated with opening of fractures under elevated pressures. The elastic component of permeability enhancement was lost during unloading (production of the well) while the shear enhancement was retained. Elastic dilation of fractures is not modeled here, although its relevance to the Desert Peak shear stimulation is discussed later.

4.2 Model setup

The computational domain comprises one eighth of a cuboid spanning 4×4 km horizontally, and 1.84 km vertically (actual dimensions 2×2×0.92 km). Injection occurs at the lower corner of the domain corresponding to the depth of major loss during stimulation; mesh resolution at the fluid egress point is 3 m. The minimum and maximum horizontal principal stresses are aligned with the X and Y axes, respectively. This ensures that off-diagonal components of the enhanced permeability tensor are very small. All model boundaries are closed to heat and mass flow except the top surface where pressure is

fixed as atmospheric. Roller boundary conditions are applied at the lateral and lower boundaries, enforcing zero normal displacement, while a no-traction boundary condition is applied at the upper boundary, corresponding to the free surface of the Earth.

Ambient vertical gradients in the principal stresses are applied as an initial condition. The magnitude of σ_v is given by the overburden, while the magnitude of σ_h was determined from a hydraulic-fracturing test to be $0.61\sigma_v$ at the top of the stimulation interval [3]. It is assumed the ratio between σ_h and σ_v is preserved with depth. The magnitude of σ_H is expected to lie somewhere between σ_v and the midpoint of σ_h and σ_v [3]; here, we use the lower bound ($\sigma_H = (\sigma_v + \sigma_h)/2$), which is consistent with the predominance of normal faulting in this area.

As in the wellbore model, initial temperatures in the reservoir are derived from a static down-hole temperature log collected before the stimulation (Figure 3B). Our initial temperature model is 1D and thus we do not account for any pre-existing horizontal variability in the temperature field such as might be expected in proximity to an operating geothermal system. Fluid pressure in the system is initially hydrostatic and corresponds to a water table 116 m below the ground surface [3]. However, approximately one year prior to the stimulation, the well was plugged to the bottom of the stimulation interval and was intermittently filled to the surface with water. Therefore, pressure in the near well region could be up to 1.1 MPa higher than modeled here.

Injection of fluid is modeled as a single source term at the lower corner node in the model domain. Water, at time-varying temperature, flows into the domain at a rate proportional to the pressure difference between the source and the node. Time-dependent source temperature and pressure are derived from the wellbore model described in Section 3.2 (Figure 7A-B); the pressure includes a density correction due to the evolution of a cold-hydrostatic column of water in the well a correction due to the 116 m distance between the wellhead and water table. These corrections amount to more than 1.5 MPa of additional overpressure during late stages of the stimulation. The model runs for the first 67 days of the stimulation, which is sufficient to capture the two low-pressure steps ($\leq$1.7 and $\leq$2.4 MPa) and the first medium pressure step (3.1 MPa). Subsequent steps are preceded by extended periods of shut-in during which time some recovery of injectivity is observed (Figure 2); as we do not account for loss of enhanced permeability, we do not model these periods of shut-in and the subsequent injection steps.

Many thermal and elastic properties of the stimulated formations at Desert Peak were constrained during a comprehensive material and reservoir characterization effort undertaken prior to the stimulation [3 7 27]. Nevertheless, there is some latitude in selecting an initial reservoir permeability

that gives a good match to the pre-damage injection rate. Furthermore, fracture failure and enhancement parameters are not tightly constrained and can be adjusted to capture the timing of injectivity increase. Finally, Δk_{max} (see Eq. (6)), the limiting permeability increase per fracture, is used to match the amount of injectivity gain. Material properties of the final calibrated model are given in Table 2.

4.3 Model results

Figure 7 summarizes down-hole temperatures and pressures and the model match to measured injection rates and injectivity for the first three pressure steps of the Desert Peak shear stimulation. Reported values of WHP and injection rate [8] were available for the first stimulation ($\leq$1.7 MPa); the model matches the injection rate of 0.2 kg s^{-1}, corresponding to a calculated injectivity of ~0.15 kg s^{-1} MPa^{-1}. During the second stimulation, a higher overpressure is applied ($\leq$2.4 MPa) resulting in a higher injection rate (~0.25 kg s^{-1}). Injectivity, measured and modeled, remains stable for these first two pressure steps as the overpressure and cooling are not sufficiently large to induce shear failure in the rock. Additionally, for the first five days of the 3.1 MPa stimulation, an increase in overpressure corresponds to a further gain in the injection rate (~0.35 kg s^{-1}), but an unchanged injectivity.

Substantial injectivity gains begin to occur approximately five to six days into the 3.1 MPa stimulation (~day 35 in Fig. 7D). During the following five days, injectivity increases by approximately a factor of 5. Accompanying the increase in injection rate is a drop in the modeled down-hole temperature from 150 to 60°C (Fig. 7A). For operational reasons, there was a three-day shut-in, during which time injectivity declined by ~0.2 kg s^{-1} MPa^{-1}. Pumping resumed for another seven days, after which a second three-day shut-in resulted in a smaller injectivity decline of ~0.1 kg s^{-1} MPa^{-1}. Sporadic pumping over the next fifteen days resulted in the measured injectivity rising to between 1.2 and 1.4 kg s^{-1} MPa^{-1}; in total, leading to an eight- to nine-fold increase over the original value.

Overall, the model match of injection rate and injectivity to observed field values during all three pressure stimulations is good. Calibration of the initial model permeability using data from the first two pressure steps and the first five days of the third pressure step ensures a reasonable match to injectivity prior to the onset of damage. The timing of damage onset between days 32 and 36 is approximately captured by the model, although the gradient of the modeled injectivity curve is steeper than the data. Modeled injectivity between days 43 and 48 are flatter than the data indicate; however, the match is improved following the second three-day shut-in, in spite of sporadic pumping. A good

match to late-time injectivity in the range of 1.2 to 1.4 kg s^{-1} MPa^{-1} is achieved using a fracture permeability multiplier of 50 ($\Delta k_{max} = 10^{50} = 1.7$).

5 Results and discussion

5.1 Near-well permeability and pressure evolution

Taking a broader view of the WHP=3.1 MPa stimulation, for an applied overpressure that varies between 3 and 4.5 MPa (Fig. 7B), the injection rate increases from 0.35 to more than 4 kg s^{-1} over a ~50 day period. Clearly, changes in permeability and fluid flow are taking place in the sub-surface. In the model, the injection rate is calculated in terms of the local permeability and the pressure difference between the well and formation. More formally, mass flow, Q, is given by

$$Q = \frac{\kappa\rho}{\mu}\nabla P, \tag{12}$$

where κ is permeability, ρ and μ are the density and viscosity of the fluid, ∇P is the pressure gradient, and the effects of gravity have been neglected. In the case that ρ and μ can be assumed constant, the rate of increase of injection rate is given by

$$\frac{dQ}{dt} = \frac{\rho}{\mu}\left(\frac{d\kappa}{dt}\nabla P + \kappa\frac{d\nabla P}{dt}\right), \tag{13}$$

i.e., there is a contribution due to (i) an increase in local permeability and (ii) a change in formation pressure gradients, i.e., $d\nabla P/dt > 0$.

While the first effect is obviously in operation – injectivity will not increase if permeability does not – we propose that the second effect also plays a role at later time. The conceptual model implemented here is that the permeability of a stimulated fracture eventually reaches some maximum value (Fig. 5), i.e., $\kappa \rightarrow \kappa_{max}$; consequently, the time derivative of permeability must tend to zero, i.e., $d\kappa/dt \rightarrow 0$ in Eq. (13). Enhanced permeability at the injection well has reached this upper limit by day 40 (Figure 8A); nevertheless, injection rates continue to rise (Fig. 7C). Setting $d\kappa/dt = 0$, and writing the near-well pressure gradient, ∇P, in terms of the pressure difference between the well, P_{well}, and the stimulated part of the reservoir, P_{res}, Eq. (13) can be rewritten

$$\frac{dQ}{dt} = \frac{\rho}{\mu}\kappa_{max}\frac{d\nabla P}{dt} = \frac{\rho}{\mu L}\kappa_{max}\left(\frac{dP_{well}}{dt} - \frac{dP_{res}}{dt}\right), \tag{14}$$

where L, is some length across which the pressure difference is measured. In the case that applied overpressure is steady, $dP_{well}/dt = 0$, in which case changes in the injection rate are due to the $-dP_{res}/dt$ term in Eq. (14). Essentially, pressures in the reservoir must decline if injection rates are to increase. In the present model, the time varying behavior of P_{well} (Fig. 7B) can make such a decline in

P_{res} difficult to detect. Nevertheless, by selecting two times with similar values for P_{well} (days 40 and 63), we show that this pressure drop indeed exists (Fig. 8A). The effect is to steepen pressure gradients near the well, thereby supporting a higher injection rate for the same nominal overpressure above the far-field reservoir pressure.

A similar pressure decline in the stimulated volume was invoked in [47] in formulating closed-form analytic solutions for the propagation of sub-surface, thermally-induced damage fronts and attendant injection rates during fixed pressure injection.

5.2 Stimulation by overpressure and "under"-temperature

Modeled profiles of formation overpressure shown in Fig. 8A illustrate the difficulty in relying on this mechanism alone for propagating a front of shear damage. In an open system, the static pressure profile for radial flow from a well at fixed pressure, has an r^{-1} dependence, i.e., pressure falls off near the well. At early time, this is not a problem, as the stimulated zone is small or non-existent and sufficiently large pressures do not need to be propagated very far to cause damage. However, as the stimulation zone grows, failure must occur at a greater distance from the well; eventually a point will be reached where the pressure drop between the well and the damage front is so large that the remaining overpressure is no longer sufficient to cause failure. At Desert Peak for example, failure is expected for ΔP_{crit} between 2.1 and 4.8 MPa ([3]; Section 2.1); however, modeled pressure profiles (Figure 8A) show that with increasing distance, the formation overpressure will eventually fall below even the lower bound of this threshold. One method to counteract this drop is to increase the WHP; essentially to displace the pressure profiles in Fig. 8A upward. However, this too, presents a challenge, as WHP is fundamentally limited by the magnitude of σ_h - if bottom-hole pressure exceeds this value, a hydraulic fracture will be formed.

Damage by thermal stressing is not as limited as that by overpressure. Inside the damage zone, due to elevated permeability, heat is advected to the damage front with very little drop in temperature. In comparison to the r^{-1} radial dependence of pressure, the temperature profile adopts the form of an error or sigmoid function (Fig. 8A, bottom panel) with relatively sharp temperature change (in comparison to pressure) taking place at the propagating damage front. Thus, the value of thermoelastic stressing – "under"-temperature – as an agent of stimulation at expanding radial distance from the injection well is preserved. Note that, at day 63, the damage front appears to have propagated much further into the formation than the low temperature front to which damage is attributed. This occurs

due to non-local stress changes associated with the large thermal strain induced around the well and is discussed in greater detail in the following section.

Accumulation of thermoelastic stress is nevertheless limited by overpressure, which directly controls the injection rate; this has two effects: (i) it controls the volume delivery rate of cold water to the formation; and (ii) it indirectly influences the temperature at which water enters the formation – faster injection rates mean less heating in the well and lower fluid temperatures going into the stimulated rock formation (Fig. 4B). The first effect controls the rate of thermoelastic stressing while the second effect controls its magnitude.

The second effect implies that initial injection rate must exceed some critical value at which water delivered to the formation is cold enough to promote stimulation, by working in concert with the direct effects of excess fluid pressure to reduce the effective normal stress across fractures favorably oriented for shearing. Some locations are sufficiently permeable (e.g., Ngatamariki geothermal field, New Zealand; [10]) that this critical injection rate is achieved at 0 WHP, i.e., formation overpressure is achieved by a depressed water table and density correction effects alone (Fig. 7B). However, at Desert Peak, the injection rate during the $\leq$1.7 and $\leq$2.4 MPa stimulations was low enough that the injectate was only 20°C cooler than ambient formation temperature when it left the well; thus, normal stress reductions across potential shear fractures were insufficient to drive these fractures into failure at these low excess fluid pressures.

A critical injection rate for thermally enhanced shear stimulation can be achieved by either increasing permeability by some other means, e.g., controlled hydraulic fracturing or acid stimulation, or by increasing the injection overpressure. In the case of Desert Peak, increasing WHP from 2.4 to 3.1 MPa sufficiently increased injection rates that shear stimulation – due to the combined effects of cooling and fluid overpressure in promoting Coulomb failure – was observed after six days. However, if initial injectivity is low enough, increasing WHP may result in uncontrolled hydraulic fracturing before this critical injection rate is achieved. Thus, preparatory stimulation treatments, e.g., acid injection or controlled hydraulic fracturing at pressures slightly in excess of σ_h, may be necessary to ensure the initial injection rate is sufficiently high to create a pervasive network of stimulated, self-propping shear fractures.

5.3 Stress changes

In the results produced by our model, changes to the total stress during stimulation are largely due to cooling caused by injection. Although overpressure is important in assessing the fracture failure criterion (Eq. (4)), it provides only a small modification to stress through the poroelastic term in the force balance. To illustrate the direct and non-local effects of cooling, in Fig. 8C we plot changes in stress components (along the same radial profile as Fig. 8A) for an optimally oriented fracture (dipping at 60° to σ_h).Thermoelastic effects are volumetric and thus their direct effect is a reduction of the normal stress. The decrease in normal stress is greatest near the wellbore where cooling is also a maximum; with increasing distance, the profile mirrors that of temperature (Fig. 8A) in producing an error function type shape. Given the relatively shallow depths at which stimulation occurs, normal stress changes of $\sim$ -30 MPa at the wellbore are sufficiently large for the rock to enter a tensile stress state (the pre-injection normal stress for the optimally oriented fracture is $\sim$ 18 MPa). Tensile failure and normal opening of fractures is not accounted for within our permeability model but would be expected to impart even larger permeability gains than those attributed to shear displacement. Furthermore, normal fracture opening by thermal contraction is a reversible process upon reheating of the formation, which may account for the partial loss of injectivity recorded at Desert Peak during periods when the well was shut-in (Section 2.3).

The induced thermal stress/strain is also responsible for non-local changes in stress that extend beyond the cooled region. Because the cooled rock is mechanically coupled to the larger rock volume, cooling at the wellbore exerts a stress on the adjacent uncooled rock. This induces horizontal extension at the injection depth, and horizontal compression above and below. Segall and Fitzgerald [48] considered fluid extraction from underground reservoirs – an analogous scenario in which rock contraction is poroelastic rather than thermoelastic – and used the elliptical inclusion method of Eshelby [49] to analyze stresses induced outside the reservoir. Their findings suggested that the non-local stress changes were large enough to trigger seismicity outside the reservoir.

In the scenario modeled here, the induced thermal stress/strain is not constant inside of some defined ellipsoid and thus the relationships derived in [48] are not directly applicable. Nevertheless, the approach is an intuitive means for conceptualizing stress changes outside the cooled region, which here be referred to as “non-local”. Profiles of shear stress change (Fig. 8C) show that this non-local stressing rises to a peak and then declines with distance from the well. The magnitude and distance of the peak from the well both increase as the stimulation proceeds and the cooled rock volume grows. At 63 days,

the induced shear stress peaks at > 7 MPa at 16 m distance from the well but remains an appreciable size out to 35 m.

Shear failure of modeled fractures is defined in Eq. (4) in terms of an excess shear stress, $\boldsymbol{\tau_{ex}}$, which contains contributions from overpressure, normal and shear stress. The relative importance of each of these three terms as a contribution to $\boldsymbol{\tau_{ex}}$ is plotted in (Figure 8D) for the same radial profile from the injection well. Immediately adjacent to the well, where cooling and thermoelastic effects are largest, the component of normal stress reduction is the dominant contribution to failure. However, from a distance of ~18 m out to the edge of the failure front (~30 m), non-local shear stress changes provide the larger contribution to failure. This is significant because it suggests that in some situations the failure front might not be advanced by the direct influence of the injected fluid – either through overpressure or thermal contraction – but rather by the non-local stress caused by the accumulating effects of injection behind the front. This scenario has implications for the rate of advance of the failure front, as the rate of pressure diffusion and heat advection will differ between the unstimulated and stimulated rock volumes.

The results of this section, particularly the spatial extent of non-local stress changes, must be interpreted with caution because the model does not account for plastic effects on the formation due to tensile failure. The theory of plasticity places a limit on the magnitude of stress changes that can be sustained by the material and, in the context of the present model, would limit the magnitude of the tensile stresses generated around the borehole. This in turn is expected to limit the extent and magnitude of non-local stresses to less than those reported by the present model. Nevertheless, non-local effects would continue to play a role in the stimulation.

5.4 Creation of a stimulated volume

The primary objective of shear stimulation is the creation of a high surface-area flow network from which injected fluids can extract heat. Therefore, the volume of rock stimulated is a key measure of the ongoing success of a stimulation operation. In our model, stimulation is not a binary description of the rock, i.e., unstimulated vs. stimulated, but rather a condition that evolves as more and more fracture orientations are activated (Fig. 5D). Therefore, the extent of stimulation must be accounted for in defining the stimulated volume; here, we use two definition: (i) partially stimulated, defined by $\boldsymbol{\Delta k_{max} > \Delta k > 0}$, i.e., permeability exhibits some enhancement; and (ii) fully stimulated, defined by $\boldsymbol{\Delta k = \Delta k_{max}}$, i.e., enhanced permeability has reached its upper limit. Stimulated volumes corresponding to these two criteria, along with the total stimulated volume, are plotted in Fig. 8B.

Consistent with the onset of significant injectivity gain (Fig. 7D), growth of the stimulated volume begins around day 37. Except for the two pumping gaps identified in Fig. 7D, growth is fairly consistent for the next thirty days of the stimulation. At the end of the WHP 3.1 MPa pressure step, the model predicts a total stimulated volume is ~20×10^3 m^3, which corresponds to an equivalent sphere of radius 24.5 m. Given that our model assumes thermal equilibration between the rock matrix and injected fluid, this number is likely an underestimate of the reservoir volume influenced by fluid injection. A dual permeability model would relax the equilibration requirement and potentially allow thermal effects to propagate further from the well; however, such modifications would add additional free parameters and thus pose additional challenges for model calibration.

Injectivity measured at the wellhead shows only moderate to small gains after around day 55 (Fig. 7D). Therefore, it is particularly interesting to note during this period that there is continued growth of the stimulated volume. In fact, we can define two metrics, related to the volume of injected fluid, that provide a better correlation with the growing volume of stimulation,

$$\boldsymbol{Q(t)} = \frac{\mathbf{1}}{\boldsymbol{\phi}} \int \boldsymbol{q(t)}\, \boldsymbol{dt}, \tag{15}$$

$$\widehat{\boldsymbol{Q}}\boldsymbol{(t)} = \frac{\mathbf{1}}{\boldsymbol{\phi}} \int \boldsymbol{q(t)} \frac{\boldsymbol{T_0 - T_{inj}(t)}}{\boldsymbol{T_0 - T_{surf}}}\, \boldsymbol{dt}, \tag{16}$$

where $\boldsymbol{q(t)}$ is the injection rate (Fig. 3D), $\boldsymbol{\phi}$ is porosity, $\boldsymbol{T_{inj}(t)}$ is the time varying injection temperature (given as $\boldsymbol{T_{out}(t)}$in Fig. 4B), $\boldsymbol{T_0}$ is the ambient formation temperature (180°C) and $\boldsymbol{T_{surf}}$=30°C represents a lower limit for $\boldsymbol{T_{inj}(t)}$. The first quantity, $\boldsymbol{Q(t)}$, is the total volume of injected fluid – the injectate – and $\widehat{\boldsymbol{Q}}\boldsymbol{(t)}$ refers to the "thermally active" injectate. In the second measure, only fluid below the ambient formation temperature is included as it operates as an agent for thermal stressing. Note that, as for stimulated rock volumes, both these quantities have been divided by porosity to represent the volume of space that this pore fluid would occupy.

There is a close correlation between $\widehat{\boldsymbol{Q}}\boldsymbol{(t)}$ and the total stimulated volume; this occurs because in our model thermoelastic stresses are the dominant factor driving failure during shear stimulation, especially away from the wellbore. Furthermore, a flattening of the injectivity curve (Fig. 7D) does not necessarily imply that the stimulated zone has stopped growing; only that pressure gradients near the well are not changing rapidly.

5.5 Model sensitivities

As discussed earlier, several aspects of the simulated injectivity curve (Fig. 7D) are sensitive to input parameters of the model. For the Desert Peak stimulation, many of these parameters are

constrained (Table 2), either by the pre-stimulation site characterization, laboratory testing on core or the results of a wellbore simulation (e.g., injection overpressure and temperature, Figure 4). Nevertheless, it is worth discussing some of the more general model sensitivities, as these illustrate the underlying physical mechanisms that control failure and injectivity enhancement.

In our conceptual model, shear stimulation occurs when the Mohr-Coulomb Failure criterion is met. Assuming that ambient stresses do not immediately satisfy the failure criterion, but rather must be perturbed toward a state of failure, then for a general system, the time at which injectivity first begins to rise will be sensitive to:

1. Ambient differential stress: loosely parameterized in a normal faulting stress regime as $\boldsymbol{\sigma_v - \sigma_h}$. The larger this quantity, the closer a system is to failure and the smaller the fluid pressure or thermo-elastic stress perturbation required to bring about changes in injectivity.
2. Material parameters present in the Mohr-Coulomb failure criterion, i.e., friction coefficient and cohesion. Larger values increase the resistance of fractures to failure, thereby requiring larger fluid pressure or stress changes before permeability enhancement occurs.
3. Injection pressure and temperature: at higher WHP, cold water is injected into the well, and delivered to the formation, at a greater rate (Figure 8C). As a result, in addition to greater reduction in effective normal stress due to rises in fluid pressure, thermoelastic stresses accumulate more rapidly. Furthermore, as the water spends less time in the well, any heating by the wellbore is minimized and colder water is delivered to the formation (Figure 4B); this increases the magnitude of thermoelastic stresses. It also increases the down-hole pressure for a given WHP – through the additional weight of a cold water column – that provides an additional boost to the injection rate and a greater reduction in effective normal stress across potential shear surfaces due to the direct fluid pressure effect.
4. Thermoelastic rock properties, i.e., Young's modulus and coefficient of thermal expansion: These control the magnitude of thermal stresses that are induced, similar to injection temperature.
5. Initial permeability/injectivity: With the excess fluid pressure, this controls the initial injection rate. A higher permeability facilitates enhanced rock cooling and greater accumulation of thermal stresses.

Many of the aforementioned parameters are material in nature and, except in choosing a site and formation to stimulate, are outside operator control. Nevertheless, constraining these parameters

through direct in-situ and laboratory testing is important for construction of a well-calibrated model and design of a wellbore stimulation procedure optimized for a particular site.

Other parameters, such as injection pressure and temperature, can be varied by an operator to achieve desired stimulation goals. In the case of Desert Peak, WHP was stepped up in increments of 0.6-0.9 MPa; as a direct result, significant stimulation was achieved for WHP 3.1 MPa.

6 Conclusion

Hydraulic well stimulation at pressures less than the minimum principal stress is increasingly commonplace in geothermal fields. The technique enhances the permeability of existing fractures through self-propping shear failure and aims to create a stimulation volume with tortuous percolation pathways and high fracture surface area. Shear stimulation applied at Desert Peak resulted in an order-of-magnitude increase in the injectivity of well 27-15.

A 2D wellbore model was constructed (Fig. 3) to describe bottom-hole temperature and pressure conditions in well 27-15 during stimulation. Results indicated that bottom-hole injection temperature varies from 180°C at early time and low injection rate to as low as 30°C for the high injection rates occurring at the end of the stimulation (Figure 4B). Cooling and density increase of the wellbore fluid also contributes to bottom-hole overpressure; the calculated correction is as large as 0.6 MPa during later stages of the stimulation.

A second model was constructed to describe injection of cold- water into the target formation, the associated effects on stress and permeability, and the injectivity evolution of well 27-15 with time. A sub-grid-scale model for fracture permeability enhancement in response to Mohr-Coulomb failure and shear displacement is used to describe permeability as a function of induced stress changes (Fig. 5). The model is constrained by measurements of ambient pressure, temperature and stress state, as well as material, mechanical and fracture properties appropriate for the stimulated formations at Desert Peak.

The well stimulation model yields a reasonable match to the injection rate and well injectivity recorded during the two low pressure and one medium pressure shear stimulations (Fig. 7). In our model, the evolving injection rate is not prescribed, but is instead determined by the time-varying bottom-hole pressure (informed by the wellbore model) and ongoing permeability enhancement. Thus, recorded injection rates provide a calibration dataset for accurate representation of near-well permeability evolution. Non-response of injectivity at low WHP is reproduced by the model; during these stages, the pressure of the injected fluid is too low, and the temperature change in the formation

not large enough, to cause shear failure. The onset of injectivity gain and final injectivity values are approximately matched although further calibration efforts may yield improvements.

The stimulated volume created around the injection interval grows steadily following the onset of injectivity gains around day 35. Interestingly, at later time when injectivity gains are so small as to be obscured by noise in the pumping data, the stimulated volume continues to grow at an appreciable rate. During this period of the stimulation, other measurement techniques, e.g., microseismic monitoring or geochemical tracer studies, may be required assess the evolution of the system.

Pressure drops off rapidly with distance from the well; at several meters, pressure is too low to cause shear failure (Fig. 8A). Nevertheless, failure continues to occur and is accompanied by ongoing propagation of the damage front into the target formation. Failure is now being promoted at relatively low excess fluid pressures by thermal and non-local stresses produced by a low temperature zone that grows around the wellbore. Further evidence that stimulation is thermally enhanced is provided by a good correlation between the volume of thermally-active injectate (Eq. (16)) and the volume of the stimulated region (Fig. 8B). However, while the direct and non-local effects of thermal contraction play a key role in propagating the damage front, the applied WHP plays an equally important role in advecting the low-temperature fluid into the formation, without which failure would not occur.

Two features of the shear stimulation not currently addressed by the model are the loss of injectivity during periods of shut-in and the absence of recorded microseismicity during the injection. These observations can be accounted for if permeability enhancement is entirely attributed to elastic dilation of fracture apertures either by pressurization or thermal contraction (and the reverse process during shut-in). While a purely elastic mechanism cannot be discounted, there are several reasons to expect that shear failure played a significant role in the stimulation. First, formation pressure, principal stress components and frictional properties of in situ fractures measured at Desert Peak predict a critical overpressure for shear failure of 2.1 to 4.8 MPa (Section 2.1), which is within the range achieved during the stimulation (2.8 to 4.8 MPa, Fig. 7B). Second, injectivity was observed to be stable for the two lower pressure steps (WHP $\leq$1.7 and $\leq$2.4 MPa) but then to abruptly increase during the WHP $\leq$3.1 MPa step; this suggests exceedance of a critical pressure threshold as required by a shear failure model. Finally, it is possible that seismicity was triggered during shear stimulation at Desert Peak but that the magnitude was below the detector threshold. For an estimated network sensitivity of M 0.2 and supposing a Brune-type earthquake model of uniform stress drop (0.1 – 10 MPa) on a circular crack, then slip on fractures of dimension 4.4 – 20.5 m would go undetected. In other words, only microearthquakes with source dimensions approaching that of the modeled stimulation zone would be detectable. Alternative

permeability recovery mechanisms to account for the loss of injectivity during periods of well shut-in include inelastic deformation or chemical sealing of the sheared fractures.

Future modifications of the model are intended to address some of the shortcomings noted here, in particular: (i) use of a hybrid elastic/shear enhancement model to address partial injectivity loss during shut-in, and (ii) use of a continuum plasticity model to avoid non-physical stresses in excess of either Mohr Coulomb or tensile failure, with permeability enhancement a function of the plastic strain tensor. Finally, a generalized parameter study, investigating aspects of the stimulation geometry, how these depend on underlying fracture properties and in-situ stresses, and how they influence optimal design of the injection operation, would provide a greater understanding of the complex stimulation process.

Acknowledgements

The authors thank Ezra Zemach for valuable discussions pertaining to Desert Peak field operations. Funding for this work was provided by US DOE Office of Geothermal Technologies under Work Authorization No. GT-1000036-12_Revision 1. The coupled flow and stress numerical simulation capabilities in FEHM applied for this work were developed at LANL under the Zero Emission Research & Technology (ZERT-II) project funded by US DOE through its CO_2 sequestration R&D program. The authors thank Jonny Rutqvist and Robert Zimmerman for helpful comments that improved the manuscript.

References

1. Barton C, Zoback M, Moos D. Fluid-flow along potentially active faults in crystalline rock. Geology 1995;23(8):683-86.

2. Townend J, Zoback M. How faulting keeps the crust strong. Geology 2000;28(5):399-402.

3. Hickman SH, Davatzes NC. In-situ stress and fracture characterization for planning of an EGS stimulation in the Desert Peak geothermal field, Nevada. 35th Workshop on Geothermal Reservoir Engineering. Stanford, CA, 2010.

4. Hickman SH, Zoback MD, Barton CA, Benoit R, Svitek J, Summers R. Stress and Permeability Heterogeneity within the Dixie Valley Geothermal Reservoir: Recent Results from Well 82-5. 25th Workshop on Geothermal Reservoir Engineering. Stanford, CA, 2000.

5. Davatzes NC, Hickman SH. The Feedback Between Stress, Faulting, and Fluid Flow: Lessons from the Coso Geothermal Field, CA, USA. World Geothermal Congress. Bali, Indonesia, 2010.

6. Henneberger R, Browne P. Hydrothermal alteration and evolution of the Ohakuri hydrothermal system, Taupo Volcanic Zone, New Zealand. Journal of Volcanology and Geothermal Research 1988;34(3-4):211-31.

7. Lutz SJ, Hickman S, Davatzes N, Zemach E, Drakos P, Robertson-Tait A. Rock Mechanical Testing and Petrologic Analysis in Support of Well Stimulation Activities at the Desert Peak Geothermal Field, Nevada. 35th Workshop on Geothermal Reservoir Engineering. Stanford, CA, 2010.

8. Chabora E, Zemach E, Spielman P, et al. Hydraulic Stimulation of Well 27-15, Desert Peak Geothermal Field, Nevada, USA. 37th Workshop on Geothermal Reservoir Engineering. Stanford, CA, 2012.

9. Garcia J, Walters M, Beall J, et al. Overview of the Northwest Geysers EGS Demonstration Project. 37th Workshop on Geothermal Reservoir Engineering. Stanford, CA, 2012.

10. Grant MA, Clearwater J, Quinao J, Bixley PF, Le Brun M. Thermal stimulation of geothermal wells: a review of field data. 38th Workshop on Geothermal Reservoir Engineering. Stanford, CA, 2013.

11. Aqui AR, Zarrouk S. Permeability Enhancement of Conventional Geothermal Wells. 33rd New Zealand Geothermal Workshop. Auckland, New Zealand, 2011.

12. Kelkar S, Lewis K, Karra S, et al. A simulator for modeling coupled thermo-hydro-mechanical processes in subsurface geological media. International Journal of Rock Mechanics and Mining Sciences 2014;70:569-80.

13. Rutqvist J, Wu Y-S, Tsang C-F, Bodvarsson GA. A Modeling Approach for Analysis of Coupled Multiphase Fluid Flow, Heat Transfer, and Deformation in Fractured Porous Rock. International Journal of Rock Mechanics and Mining Sciences 2002;39(4):429-42.

14. Kolditz O, Bauer S, Bilke L, et al. OpenGeoSys: an open-source initiative for numerical simulation of thermo-hydro-mechanical/chemical (THM/C) processes in porous media. Environmental Earth Sciences 2012;67(2):589-99.

15. Taron J, Hickman S, Ingebritsen SE, Williams C. Using a fully coupled, open-source THM simulator to examine the role of thermal stresses in shear stimulation of enhanced geothermal systems. 48th US Rock Mechanics/Geomechanics Symposium. Minneapolis, MN, 2014.

16. Podgorney R, Huang H, Gaston D. Massively parallel fully coupled implicit modeling of coupled thermal-hydrological-mechanical processes for enhanced geothermal system reservoirs. 35th Workshop on Geothermal Reservoir Engineering. Stanford, CA, 2010.

17. Nathenson M. The dependence of permeability on effective stress from flow tests at hot dry rock reservoirs at Rosemanowes (Cornwall) and Fenton Hill (New Mexico). Geothermics 1999;28(3):315-40.

18. Bai M, Meng F, Elsworth D, Roegiers J. Analysis of stress-dependent permeability in nonorthogonal flow and deformation fields. Rock Mechanics and Rock Engineering 1999;32(3):195-219.

19. Hossain M, Rahman M, Rahman S. A shear dilation stimulation model for production enhancement from naturally fractured reservoirs. SPE Journal 2002;7(2):183-95.

20. Rutqvist J, Leung C, Hoch A, Wang Y, Wang Z. Linked multicontinuum and crack tensor approach for modeling of coupled geomechanics, fluid flow and transport in fractured rock. Journal of Rock Mechanics and Geotechnical Engineering 2013;5(1):18-31.

21. Rinaldi AP, Rutqvist J, Sonnenthal EL, Cladouhos TT. Coupled THM Modeling of Hydroshearing Stimulation in Tight Fractured Volcanic Rock. Transport in Porous Media 2014:1-20

22. Kelkar S, Lewis K, Hickman S, Davatzes DC, Moos D, Zyvoloski G. Modeling Coupled Thermal-Hydrological-Mechanical Processes During Shear Stimulation of an EGS Well. 37th Workshop on Geothermal Reservoir Engineering. Stanford, CA, 2012.

23. Modeling Shear Stimulation of the Desert Peak EGS Well 27-15 Using a Coupled Thermal-Hydrological-Mechanical Simulator. 47th US Rock Mechanics/Geomechanics Symposium; 2013; San Francisco, CA.

24. Dempsey D, Kelkar S, Davatzes N, Hickman S, Moos D, Zemach E. Evaluating the Roles of Thermoelastic and Poroelastic Stress Changes in the Desert Peak EGS Stimulation. 39th Workshop on Geothermal Reservoir Engineering. Stanford, CA, 2014.

25. Faulds JE, Coolbaugh MF, Benoit D, et al. Structural Controls of Geothermal Activity in the Northern Hot Springs Mountains, Western Nevada: The Tale of Three Geothermal Systems (Brady's, Desert Peak and Desert Queen). Geothermal Resources Council Transactions 2010;34:675-83

26. Swyer MW, Davatzes NC. Evaluating the Role of the Rhyolite Ridge Fault System in the Desert Peak Geothermal Field with Robust Sensitivity Testing Through Boundary Element Modeling and Likelihood Analysis. 38th Workshop on Geothermal Reservoir Engineering. Stanford, CA, 2013.

27. Davatzes NC, Hickman SH. Stress and Fluid Flow Prior to Stimulation of Well 27-15, Desert Peak, Nevada, EGS Project. 34th Workshop on Geothermal Reservoir Engineering. Stanford, CA, 2009.

28. Rose P, Leecaster K, Drakos P, Robertson-Tait A. Tracer Testing at the Desert Peak EGS Project. Geothermal Resources Council Transactions 2009;33:241-44

29. Zemach E, Drakos P, Robertson-Tait A, Lutz SJ. Feasibility Evaluation of an "In-Field" EGS Project at Desert Peak, Nevada, USA. Proceedings of the World Geothermal Congress. World Geothermal Congress. Bali, Indonesia, 2010.

30. Faulds JE, Garside LJ, Oppliger GL. Structural Analysis of the Desert Peak-Brady Geothermal Fields, Northwestern Nevada: Implications for Understanding Linkages between Northeast-Trending Structures

and Geothermal Reservoirs in the Humboldt Structural Zone. Geothermal Resources Council Transactions 2003;27:859-64

31. Jaeger JC, Cook NGW, Zimmerman RW. Fundamentals of Rock Mechanics. Oxford: Blackwell; 2007.

32. Gangi A. Variation of whole and fracture porous rock permeability with confining pressure. International Journal of Rock Mechanics and Mining Sciences 1978;15(5):249-57.

33. Beeler N, Hickman S. Stress-induced, time-dependent fracture closure at hydrothermal conditions. Journal of Geophysical Research-Solid Earth 2004;109(B2).

34. Martin J, Lowell R. Precipitation of quartz during high-temperature, fracture controlled hydrothermal upflow at ocean ridges: Equilibrium versus linear kinetics. Journal of Geophysical Research-Solid Earth 2000;105(B1):869-82.

35. Morrow C, Moore D, Lockner D. Permeability reduction in granite under hydrothermal conditions. Journal of Geophysical Research-Solid Earth 2001;106(B12):30551-60.

36. Zyvoloski GA, Robinson BA, Dash ZV, Trease LL. Models and Methods Summary for the FEHM Application: Los Alamos National Laboratory, 1999.

37. Zyvoloski G. FEHM: A control volume finite element code for simulating subsurface multi-phase multi-fluid heat and mass transfer. Los Alamos: Los Alamos National Laboratory, 2007.

38. Harr L, Gallagher J, Kell GS. NBS/NRC Steam Tables, Thermodynamics, and Transport Properties and Computer Programs for Vapor and Liquid States of Water. New York: Hemisphere Press, 1984.

39. Moos D, Barton C. Modeling uncertaintly in the permeability of stress-sensitive fractures. 42nd US Rock Mechanics Symposium. San Francisco, CA, 2008.

40. McGarr A. On relating apparent stress to the stress causing earthquake fault slip. Journal of Geophysical Research-Solid Earth 1999;104(B2):3003-11.

41. McClure MW, Horne RN. Discrete Fracture Modeling of Hydraulic Stimulation in Enhanced Geothermal Systems. 35th Workshop on Geothermal Reservoir Engineering. Stanford, CA, 2010.

42. McClure MW, Horne RN. Investigation of Injection-Induced Seismicity Using a Coupled Fluid Flow and Rate/State Friction Model. 37th Workshop on Geothermal Reservoir Engineering. Stanford, CA, 2012.

43. Lee H, Cho T. Hydraulic characteristics of rough fractures in linear flow under normal and shear load. Rock Mechanics and Rock Engineering 2002;35(4):299-318.

44. Terghazi K. Theoretical Soil Mechanics. New York: John Wiley and Sons, 1943.

45. Sibson R. Structural permeability of fluid-driven fault-fracture meshes. Journal of Structural Geology 1996;18(8):1031-42.

46. Moos D, Vassilellis G, Cade R, et al. Predicting Shale Reservoir Response to Stimulation in the Upper Devonian of West Virginia. SPE Annual Technical Conference. Denver, CO, 2011.

47. Lewis K, Karra S, Kelkar S. A Model for Tracking Fronts of Stress-Induced Permeability Enhancement. Transport in Porous Media 2013;99(1):17-35.

48. Segall P, Fitzgerald SD. A note on induced stress changes in hydrocarbon and geothermal reservoirs. Tectonophysics 1998;289(1):117-28.

49. Eshelby JD. The determination of the elastic field of an ellipsoidal inclusion, and related problems. Proceedings of the Royal Society of London A: Mathematical, Physical and Engineering Sciences 1957;241(1226);376-96.

50. Robertson-Tait A, Lutz SJ, Sheridan J, Morris CL. Selection of an interval for massive hydraulic stimulation in well DP 23-1, Desert Peak East EGS project, Nevada. 29th Workshop on Geothermal Reservoir Engineering. Stanford, CA, 2004.

Figure captions

Figure 1: (A) Map of the Desert Peak geothermal field showing injection and production wells, EGS stimulation well 27-15 and geothermal power plant (purple rectangle) along with inferred faults [26 30] and the direction of the maximum horizontal principal stress (σ_H; [27 50]). (B) Stress magnitudes versus depth in well 27-15 [3]. Vertical stress (σ_V) was calculated from cuttings analysis and density measurements on core from a nearby well, least horizontal principal stress (σ_h, red square) was measured by a mini-hydraulic fracturing test, and ambient formation fluid pressure (P, relative to a water table at 115 m depth) was determined from a static, equilibrated temperature/pressure survey. The anticipated range of σ_H magnitudes is shown for a transitional normal faulting to strike-slip faulting regime. The critical horizontal stress at which normal faulting failure should occur is shown by the red shaded region for bounding values of coefficient of friction ($\boldsymbol{\mu}$) of 0.6 and 1.0. The open-hole region corresponding to the shear stimulation is shown by a pink box. Both wellbore and stimulation models extend to 1030 m depth (center of the fluid loss interval during shear stimulation; [8]), although the stimulation model begins at the water table while the wellbore model extends to the ground surface.

Figure 2: Summary of injection rate (blue) and calculated injectivity based on measured WHP (black) during the shear stimulation. Dotted lines demarcate stimulation and shut-in periods. The five pressure steps are spanned by arrows with the upper limit of applied WHP marked above each. Only reported values (open squares) are available for the $\leq$1.7 MPa pressure step.

Figure 3: Set up and inputs for the wellbore model. (A) Schematic showing modeled components (with widths) of the wellbore, as well as fluid entry and exit points. Material properties for the each of the zones are given in Table 1. The blue arrow shows the passage of the wellbore fluid. (B) Static down-hole temperature profile used as an initial temperature, $\boldsymbol{T_0}$, distribution for both the wellbore and stimulation models. (C) Surface injection temperature, $\boldsymbol{T_{in}(t)}$, and (D) injection rate, $\boldsymbol{q(t)}$, with time. These are applied as fluid entry boundary conditions in (A). Duration of the three pressure stimulations are indicated by dotted lines in (D).

Figure 4: Summary of results from the wellbore model. (A) Initial down-hole temperature profile (black), the calibrated match between the model (solid) and observation (dashed) for a static temperature profile taken after a 12-day shut-in period (red), and then shortly after a short injection test (blue). The main fluid loss interval is shaded pink. (B) Modeled bottom-hole temperature (red solid). Approximate

surface injection temperature is given by the dashed red line. On the same horizontal axes is plotted the additional overpressure at the depth of the stimulation interval, arising from the hydrostatic weight of a cooler, denser fluid column in the wellbore (blue solid). The ≤1.7, ≤2.4 and ≤3.1 MPa stimulation intervals are marked for reference.

Figure 5: Summary of stress-permeability model (A). Equal-area stereonets showing poles to planes for the fracture population observed in image logs over the Desert Peak stimulation interval (blue triangles; [27]), and several synthetic fracture populations (red circles), generated from (A) using the algorithm described in Section 4.1. The orientation of $\boldsymbol{\sigma_h}$ is shown for the Desert Peak fractures. (B) Fracture permeability versus shear displacement for laboratory tests on granite at three normal stresses, from [43]. (C) Modeled curve (Eq. (6)), with $\boldsymbol{\Delta k_{max}}$=1.7, $\boldsymbol{u_5}$= 1 mm and $\boldsymbol{u_{95}}$=7 mm. Dashed lines divide regions defining fractures that are unstimulated ($\boldsymbol{\Delta k < 0.05\Delta k_{max}}$), partially stimulated ($\boldsymbol{0.05\Delta k_{max} < \Delta k < 0.95\Delta k_{max}}$), and fully stimulated ($\boldsymbol{0.95\Delta k_{max} < \Delta k}$). Note that because $\boldsymbol{\Delta k}$ is used as a multiplier, there is no requirement that the y-intercepts of (B) and (C) coincide. (D-E) Multipliers of permeability components parallel to $\boldsymbol{\sigma_v}$ (red), $\boldsymbol{\sigma_H}$ (blue) and $\boldsymbol{\sigma_h}$ (black) for increasing normal stress reduction for the Desert Peak fracture population. Stereonets show unstimulated (green), partially stimulated (blue) and fully stimulated fractures (black) at three points on the curve. The orientation of $\boldsymbol{\sigma_h}$ is shown by black arrows. (E) The same curves as in D, but for 20 synthetic fracture populations constructed from the Desert Peak fracture population.

Figure 6: Set up and initial conditions for the stimulation model. (A) Schematic representation of the model grid in one eighth symmetry. Injection occurs into the bottom corner node contained within a high-resolution section of the grid. No flow and roller boundary condition are applied at all boundaries except the top surface, which is free to deform and fixed at atmospheric pressure. Orientation of the principal stresses relative to the coordinate axes is indicates in the top right. (B) Depth-dependent pressure, stress components and temperature applied as an initial condition. Initially, there is no horizontal variability in these variables.

Figure 7: Summary of the calibrated reservoir stimulation model. Model inputs: (A) Down-hole injection temperature. (B) Components of the down-hole injection pressure. Model outputs: (C) Injection rate. (D) Injectivity calculated based on WHP. Field data are indicated by circles and modeled values by solid lines. Reported values (open squares) of overpressure and injection rate are obtained for the ≤1.7 MPa stimulation from [8]. The maximum formation overpressure that would result in a hydraulic fracture is

indicated by a gray dashed line in (B). The positions of two pumping gaps are marked in (D) with loss of injectivity during the gap indicated by a dotted line. Stimulation intervals for the three lower pressure steps are indicated in (A) and marked by vertical dotted lines.

Figure 8: Summary of modeled flow, stress and permeability changes during the stimulation. (A) Change in permeability (black), formation overpressure (blue) and temperature (red) for a profile along the x-axis at three times: (i) before stimulation begins (dotted line); (ii) during the WHP=3.1 MPa pressure step, prior to the first pumping gap (40 days – dashed line); (iii) 23 days later during the same pressure step (63 days – solid line). Arrow shows movement of the damage front ~10 m from day 40 to day 63. (B) Increase in the stimulated volume with time for the 3.1 MPa stimulation. The partially and fully stimulated volumes are defined in terms of the extent to which nodal permeability has been increased: partially = $\boldsymbol{\Delta k > 0}$, fully = $\boldsymbol{\Delta k = \Delta k_{max}}$; these regions are also illustrated in relation to the permeability curves given in (A). Also shown are the total (green) and "thermally active" injectate (blue) defined in Eqs. (15) and (16), respectively. Note that both fluid and rock volumes have been scaled to represent the spatial volume occupied by the particular component, e.g., fluid volumes were divided by the porosity, $\boldsymbol{\phi}$ (=0.1), rock volumes by $(\mathbf{1} - \boldsymbol{\phi})$. (C) Components of change in normal (black), shear (green) and excess shear stress (red) along the same profile for a well-oriented fracture in the extensional stress regime (dipping at 60° to $\boldsymbol{\sigma_h}$). Change in excess shear stress is defined in terms of Eq. (4), i.e., $\boldsymbol{\Delta\tau_{ex} = \Delta|\tau| - \mu_s\Delta\sigma_n + \mu_s\Delta P}$. (D) Percentage contributions of overpressure (blue), normal (black) and shear stress change (green) to the excess shear stress. Two regions are defined where either thermal or non-local effects dominate fracture failure.

Tables

Table 1: Material parameters used in the wellbore model.

Parameter	Value
Operational	
Initial temperature	as in Figure 3B
Injection depth	1030 m
Injection temperature	as in Figure 3C

Injection rate	as in Figure 3D
Material: Wellbore	
Permeability	5^{-9} m^2
Porosity	1
Steel pipe	
Thermal conductivity	20 W m^{-1} K^{-1}
Density	8000 kg m^{-3}
Specific heat capacity	500 J m^{-3} K^{-1}
Porosity	0
Cement/reservoir	
Thermal conductivity	2.7 W m^{-1} K^{-1}
Density	2500 kg m^{-3}
Specific heat capacity	800 J m^{-3} K^{-1}
Porosity	0

Table 2: Parameters used in the stimulation model.

Parameter	Value
Operational	
Injection depth	1035 m
Injection pressure	as in Figure 7A
Injection temperature	as in Figure 4A
Material	
Thermal conductivity	2.7 W m^{-1} K^{-1}
Density [7]	2477 kg m^{-3}
Specific heat capacity	800 J m^{-3} K^{-1}
Porosity [7]	0.1

Coefficient of thermal expansion	3.5×10^{-5} K^{-1}
Young's mod. [7]	25 GPa
Poisson's ratio [7]	0.2
Reservoir	
Reservoir temperature	as in Figure 3B
Initial permeability [X, Y, Z]	1.0, 1.2, 0.9×10^{-15} m^2
Vertical stress gradients	
σ_v (σ_Z)	ρg
σ_h (σ_X) [3]	$0.61\sigma_v$
σ_H (σ_Y)	$0.5(\sigma_v + \sigma_h)$
Fracture	
Fractures per control volume, N	100
$u_5, u_{95}, \Delta k_{max}$ [43]	1, 7 mm, 1.7 log(m^2)
Cohesion, S_0	0. MPa
Static friction, μ_s [7]	0.75
Dynamic friction, μ_d [40]	0.65
Shear fracture stiffness, K_s	5×10^2 MPa m^{-1}

highlights

Shear stimulation by cold water injection improved injectivity of well DP 27-15

A model of permeability enhancement due to shear failure is developed for DP 27-15

Thermal stress contributes more to failure as damage propagates away from borehole

Stimulated volume correlates well to cold injectate volume, poorly with injectivity

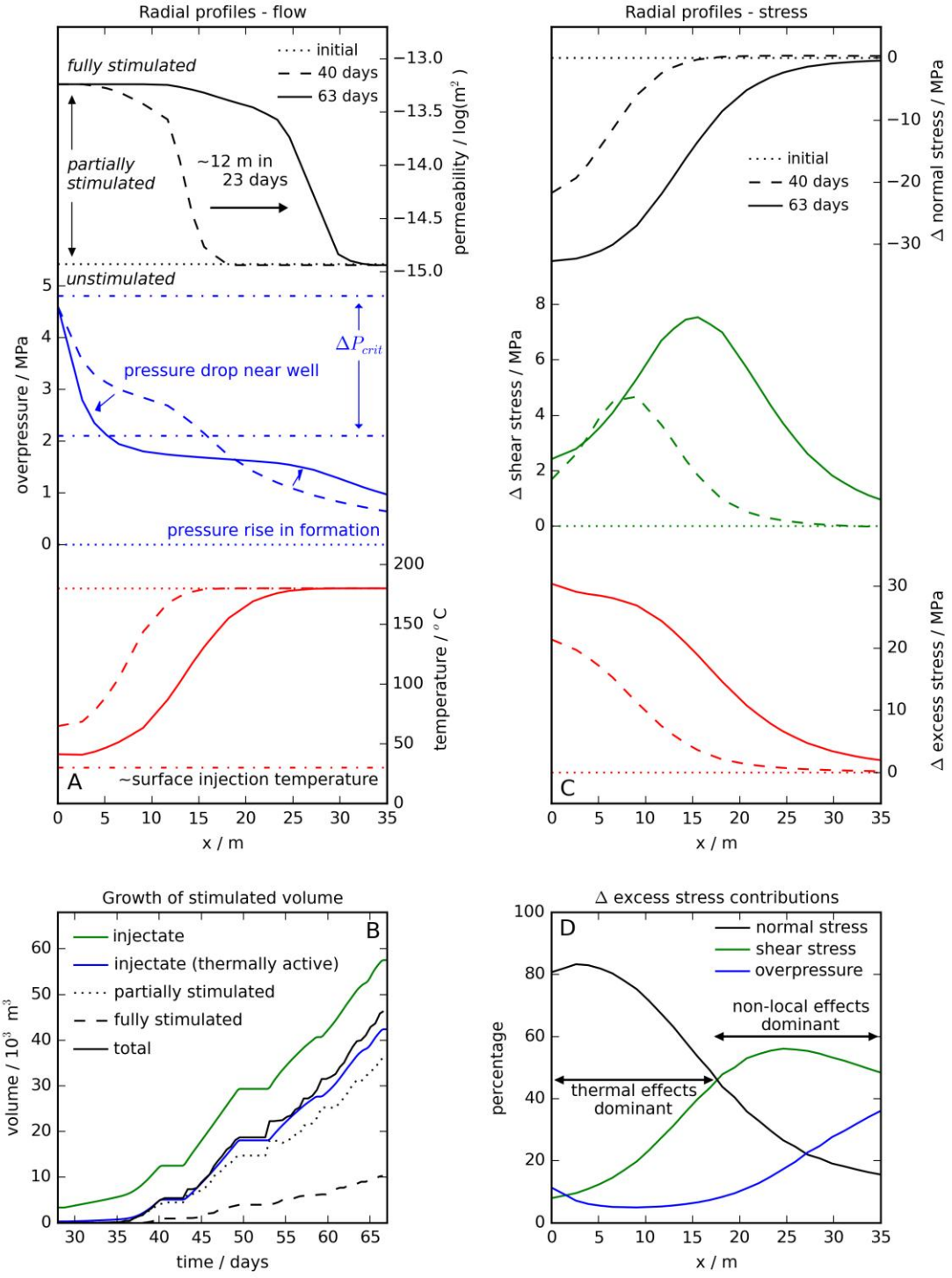
Radial profiles - flow
initial
40 days
63 days
fully stimulated
partially stimulated
~12 m in 23 days
unstimulated
ΔP_{crit}
pressure drop near well
pressure rise in formation
overpressure / MPa
permeability / log(m^2)
temperature / °C
A
~surface injection temperature
x / m
Radial profiles - stress
Δ normal stress / MPa
Δ shear stress / MPa
Δ excess stress / MPa
C
Growth of stimulated volume
injectate
injectate (thermally active)
partially stimulated
fully stimulated
total
B
volume / 10^3 m^3
time / days
Δ excess stress contributions
D
normal stress
shear stress
overpressure
non-local effects dominant
thermal effects dominant
percentage

Fig. 1

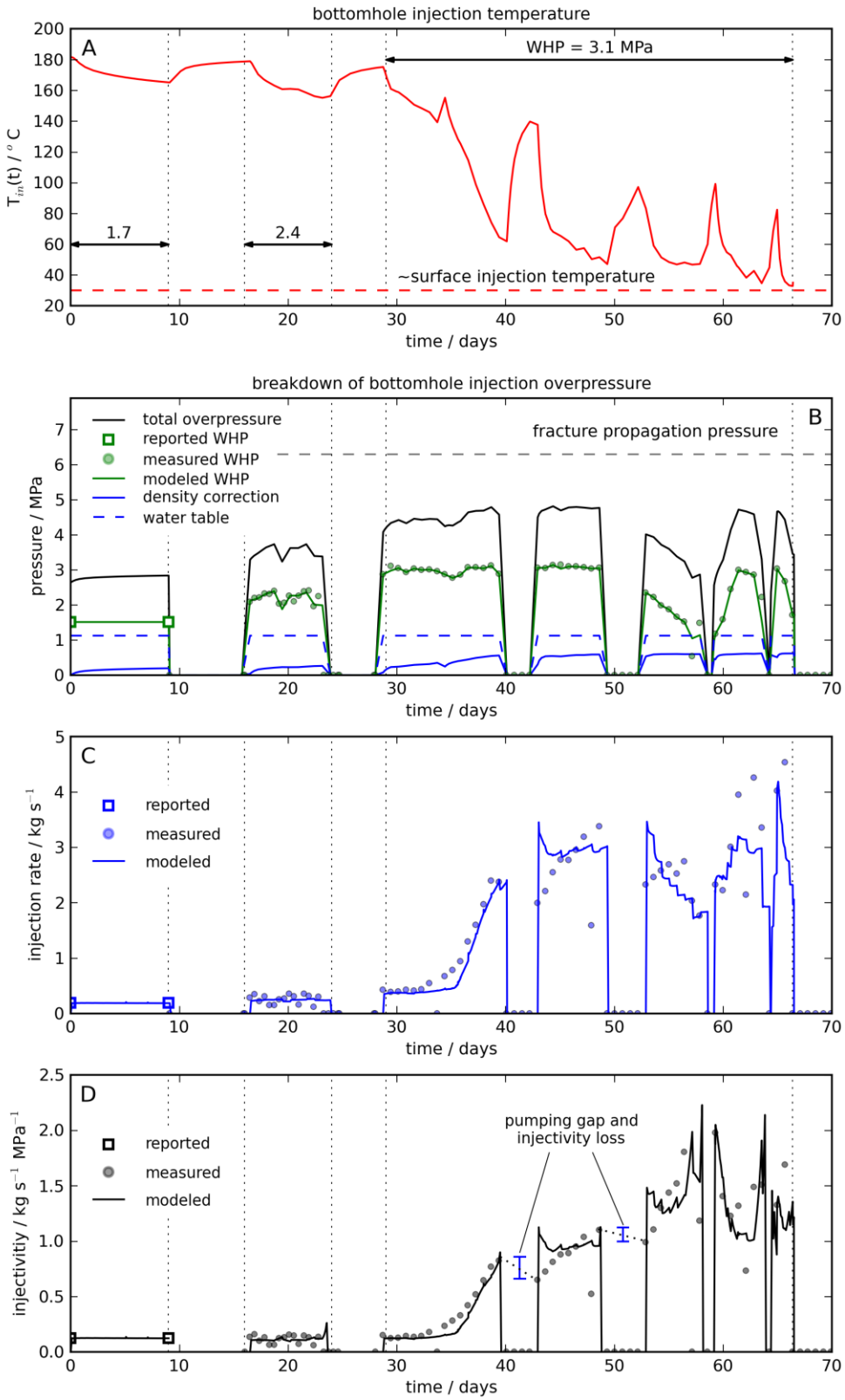
bottomhole injection temperature
A
WHP = 3.1 MPa
1.7
2.4
~surface injection temperature
$T_{in}(t)$ / ^{o} C
time / days
breakdown of bottomhole injection overpressure
total overpressure
reported WHP
measured WHP
modeled WHP
density correction
water table
fracture propagation pressure
B
pressure / MPa
time / days
C
reported
measured
modeled
injection rate / kg s^{-1}
time / days
D
reported
measured
modeled
pumping gap and
injectivity loss
injectivitiy / kg s^{-1} MPa^{-1}
time / days

Fig. 2

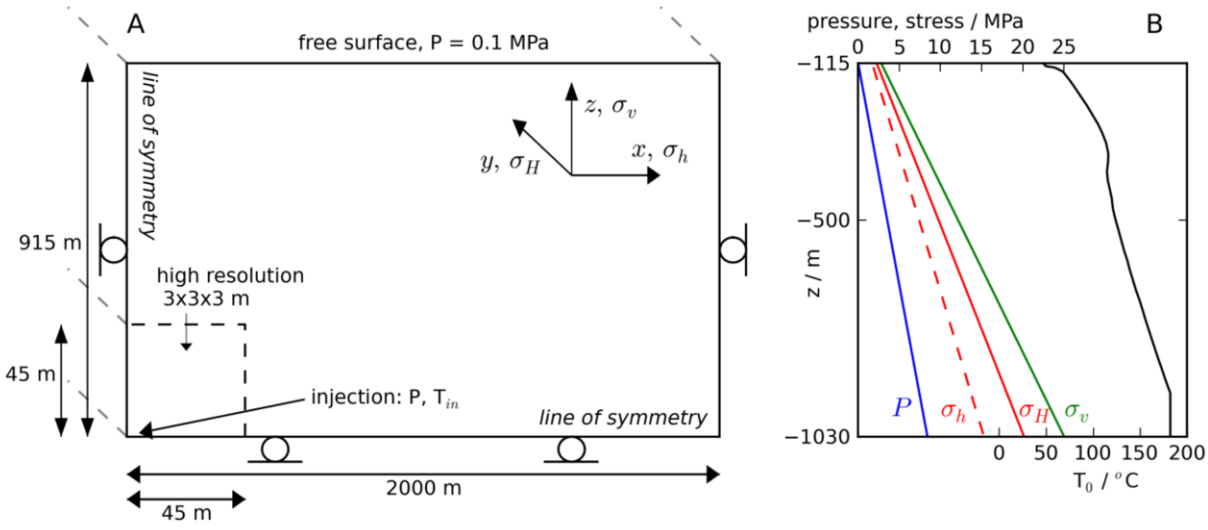
A
free surface, P = 0.1 MPa
line of symmetry
z, σ_v
x, σ_h
y, σ_H
915 m
high resolution
3x3x3 m
45 m
injection: P, T_{in}
line of symmetry
2000 m
45 m
pressure, stress / MPa
B
0 5 10 15 20 25
−115
−500
−1030
z / m
P
σ_h
σ_H
σ_v
0 50 100 150 200
T_0 / °C

Fig. 3

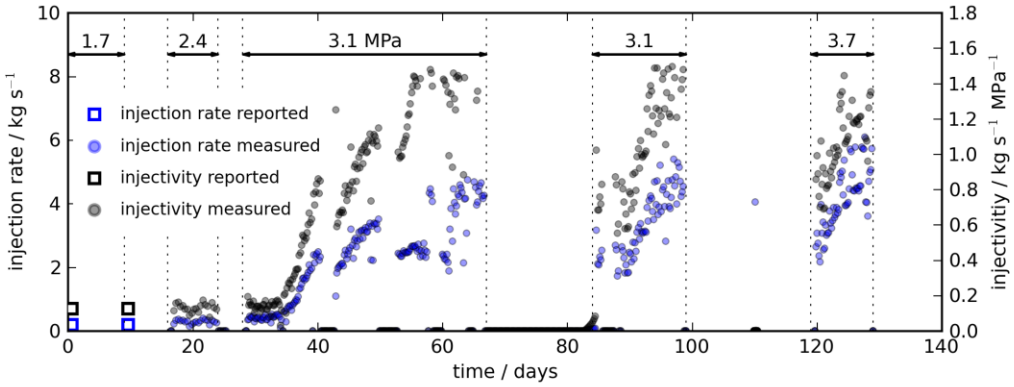
1.7
2.4
3.1 MPa
3.1
3.7
injection rate reported
injection rate measured
injectivity reported
injectivity measured
injection rate / kg s⁻¹
injectivitiy / kg s⁻¹ MPa⁻¹
time / days
0
20
40
60
80
100
120
140
0
2
4
6
8
10
0.0
0.2
0.4
0.6
0.8
1.0
1.2
1.4
1.6
1.8

Fig. 4

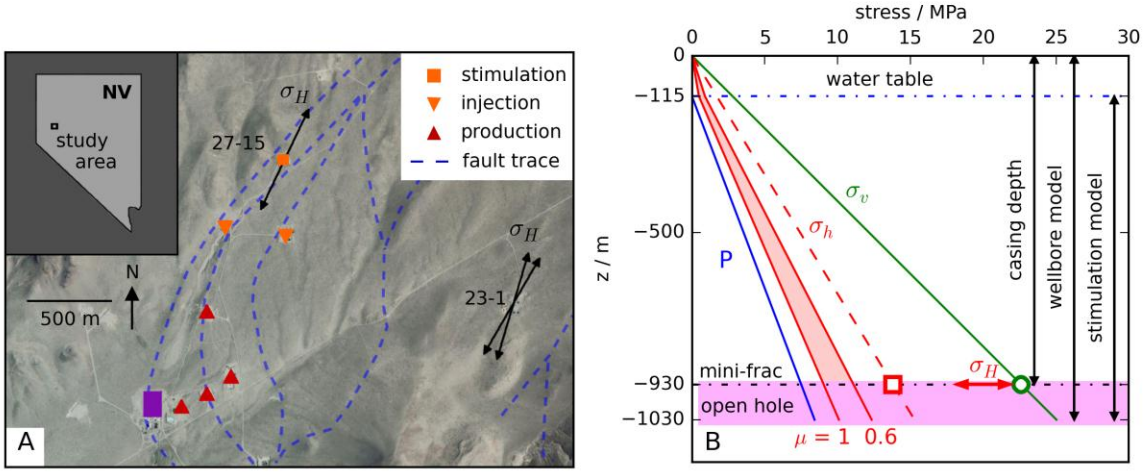
NV
study area
N
500 m
A
σ_H
27-15
σ_H
23-1
stimulation
injection
production
fault trace
stress / MPa
0
5
10
15
20
25
30
water table
−115
−500
−930
−1030
z / m
σ_v
σ_h
P
casing depth
wellbore model
stimulation model
mini-frac
open hole
σ_H
$\mu = 1$ 0.6
B

Fig. 5

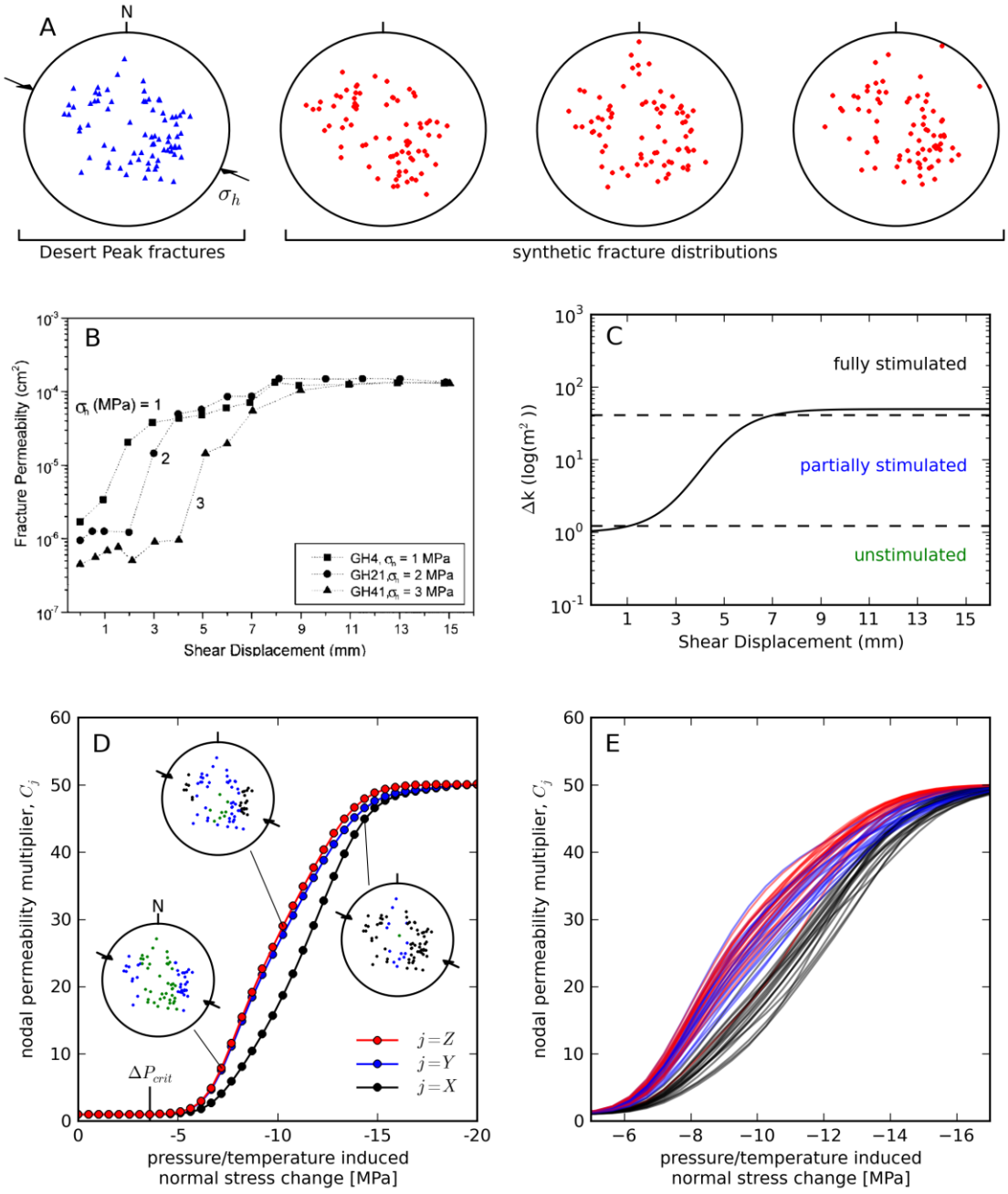
A
N
σ_h
Desert Peak fractures
synthetic fracture distributions
B
Fracture Permeability (cm²)
σ_n (MPa) = 1
2
3
GH4, σ_n = 1 MPa
GH21,σ_n = 2 MPa
GH41,σ_n = 3 MPa
Shear Displacement (mm)
C
Δk (log(m²))
fully stimulated
partially stimulated
unstimulated
Shear Displacement (mm)
D
nodal permeability multiplier, C_j
N
ΔP_{crit}
$j=Z$
$j=Y$
$j=X$
pressure/temperature induced
normal stress change [MPa]
E
nodal permeability multiplier, C_j
pressure/temperature induced
normal stress change [MPa]

Fig. 6

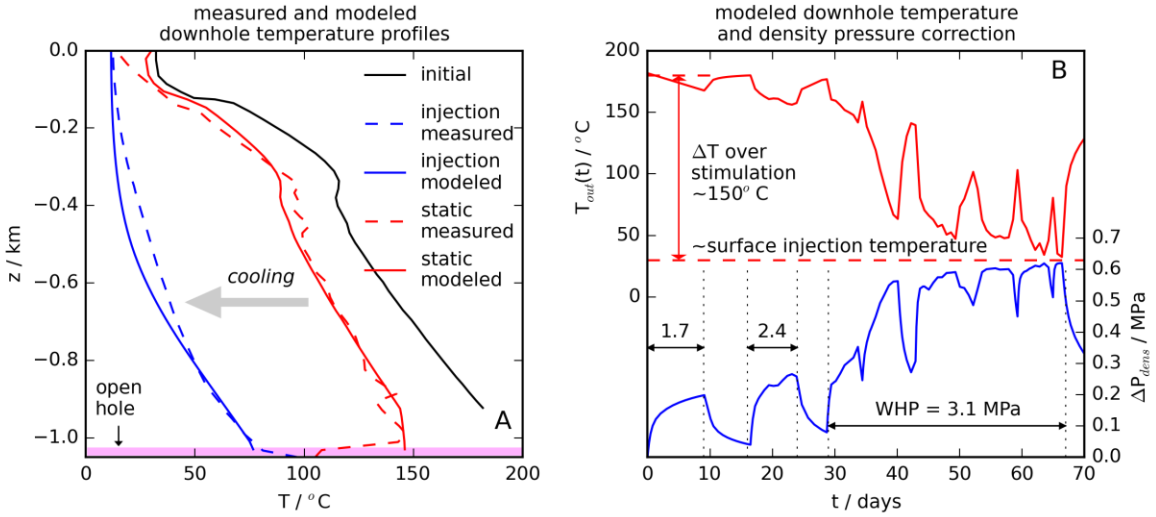
measured and modeled
downhole temperature profiles
initial
injection
measured
injection
modeled
static
measured
static
modeled
cooling
open
hole
A
z / km
T / °C
modeled downhole temperature
and density pressure correction
B
ΔT over
stimulation
~150° C
~surface injection temperature
1.7
2.4
WHP = 3.1 MPa
t / days
ΔP_dens / MPa

Fig. 7

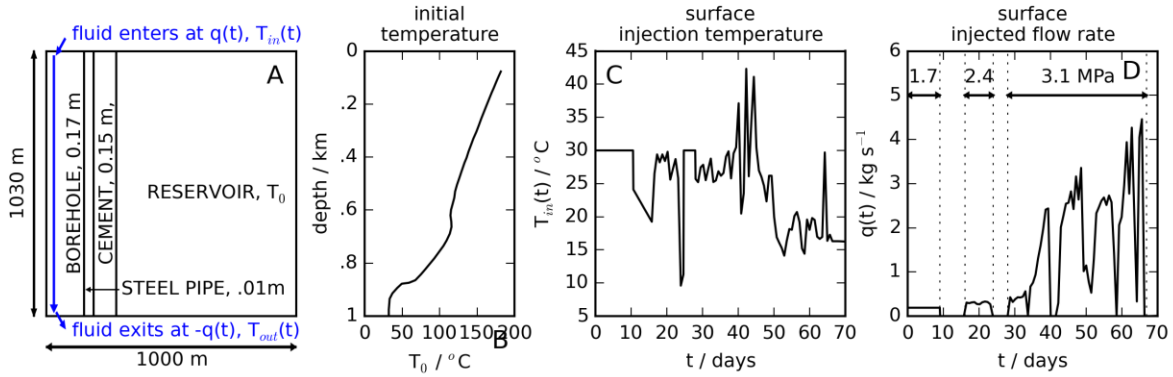
fluid enters at q(t), T_{in}(t)
A
1030 m
BOREHOLE, 0.17 m
CEMENT, 0.15 m,
RESERVOIR, T_0
STEEL PIPE, .01m
fluid exits at -q(t), T_{out}(t)
1000 m
initial
temperature
depth / km
T_0 / °C
B
surface
injection temperature
C
T_{in}(t) / °C
t / days
surface
injected flow rate
1.7
2.4
3.1 MPa
D
q(t) / kg s^{-1}
t / days

Fig. 8